Low temperature growth of ZnO thin films by filtered cathodic vacuum arc technique

Lee, Hiong Weng

2005

Lee, H. W. (2005). Low temperature growth of ZnO thin films by filtered cathodic vacuum arc technique. Master’ s thesis, Nanyang Technological University, Singapore.

https://hdl.handle.net/10356/4572

https://doi.org/10.32657/10356/4572

Low Temperature Growth Of ZnO Thin Films By Filtered Cathodic Vacuum Arc Technique

Lee Hiong Weng

School of Electrical & Electronic Engineering

A thesis submitted to the Nanyang Technological University
in fulfillment of the requirement for the degree of
Master of Engineering

2005

SUMMARY

A detailed study of zinc oxide (ZnO) films prepared by filtered cathodic vacuum arc technique (FCVA) was carried out, with an emphasis on the application of ZnO as a transparent conductive oxide (TCO), as well as the fabrication of a ZnO-based transparent thin film transistor (TFT). The films were characterized in the following aspects: structural, electrical and optical properties.

Under specific deposition conditions, it is possible to obtain films that exhibit both qualities of high optical transmittance (~90%) and low resistivity (8×10^{-4} Ωcm), thus demonstrating the feasibility of using ZnO prepared by FCVA as a TCO. X-ray diffraction results showed that even films deposited at temperatures below 150°C possessed good crystalline quality, thus indicating the suitability of its application on polymer substrates. An electronic device was fabricated using ZnO as the active layer, which yielded the transfer characteristics of an enhancement mode TFT.

ACKNOWLEDGEMENTS

First and foremost, I would like to thank Assoc Prof Lau Shu Ping for his guidance, instruction, and words of encouragement. Furthermore, I would like to express my gratitude towards Assoc Prof Tay Beng Kang for his support as the Laboratory Supervisor. Special thanks goes out to the lab technicians, Mdm Neo, Miss Janet, and Mr Hasman. I would also like to thank Dr Wang Yu Guang who provided much insight into the research topic. Finally, I would like to acknowledge Nanyang Technological University for providing the funds that made this endeavor possible.

Table of Contents

List of Figures

List of Tables

Chapter 1

Introduction

1.1 Motivation And Objectives

The motivation for this thesis is to demonstrate the suitability of the Filtered Cathodic Vacuum Arc (FCVA) technique for the growth of good quality ZnO thin films. The objectives of this thesis are: (1) the application of ZnO as transparent conducting oxide films, and (2) a preliminary study to lay the foundation for the fabrication of a ZnO-based TFT using FCVA technique.

Zinc oxide is characterized by interesting semiconductive, photoconductive, piezoelectric, acousto-optical and electro-optical properties that render it suitable for many applications. It is used as varistors [1], acoustoelectric devices [2], transparent conductors [3], phosphor [4] and gas sensors.[5] It is widely accepted that ZnO is the most promising material for realizing an ultraviolet laser at room temperature due to its wide direct band gap (E_g = 3.3eV) with a large excitonic binding energy of 60 meV at room temperature.[6, 7, 8]

Significantly high residual stress, however, may arise in the film deposited. In microelectronics and thin-film technology it is well known that mechanical stress influences not only the mechanical stability of thin-film structures but also the electrical

parameters. There is thus a need to establish a thorough understanding of the stress in the film. Since the film structure and/or orientation may vary with different processing conditions, such as substrate temperature, total gas pressure, and substrate bias, the stress in the film may also change accordingly.

To obtain high quality ZnO thin films, a variety of techniques may be used such as molecular-beam epitaxy (MBE) [9], metalorganic chemical vapor deposition (MOCVD) [10], magnetron sputtering [11, 12], and pulsed laser deposition [13] for example. High quality ZnO films are usually grown at relatively high substrate temperatures varying from 450°C to 750°C by MBE and MOCVD on sapphire substrates. In the filtered cathodic vacuum arc technique, films are deposited at lower temperatures, and this is desirable for the applications on polymer substrates, which cannot withstand high temperatures.

1.2 Major Contribution of the Thesis

A systematic study of ZnO thin films deposited using the FCVA technique was carried out. The areas of characterization performed on the films included: internal stress, crystalline quality, surface morphology, electrical properties, optical transmission, and photoluminescence. All these were done to lay the foundation for two applications:

- Use of ZnO as a transparent conducting oxide (TCO), especially on plastic substrates.
- Fabrication of ZnO-based transparent thin film transistors

The viability of using ZnO as a TCO has been demonstrated, as our films are both highly transparent and conductive, with transmittance of about 90% in the visible spectrum, and a minimum resistivity of 8×10^{-4} Ωcm was achieved.

Furthermore, it is possible to obtain good quality ZnO thin films even when deposition was performed at room temperature, hence permitting the growth of ZnO on polymer substrate. A significant advantage of the FCVA system is that even films grown at room temperature were dense films without voids, and XRD results indicated they were of reasonably good quality.

An n-channel enhancement mode thin film transistor was fabricated using ZnO as the channel layer. This is, to the best of the author's knowledge, the first time a cathodic arc deposition technique of any kind was used to fabricate a transistor. The feasibility of using FCVA to fabricate a thin film transistor had been demonstrated, although the performance of the TFT needs to be improved as this is only the first attempt.

1.3 Organization of the Thesis

The results mentioned above are provided in this thesis, which is structured as follows.

- Chapter 2 contains a review of the relevant literature on the growth of ZnO and provides an overview of the FCVA technique. This provides the technical foundation upon which a discourse of the experimental results can be built.
- Chapter 3 describes the fabrication process in the growth of ZnO thin films, and discusses the influence of deposition parameters on growth rate.

- Chapter 4 gives an overview of the various characterization techniques used to study the ZnO films, providing introductory information on the characterization equipment.
- Chapter 5 provides a discussion of the experimental results in the following aspects: structural properties, electrical properties, optical properties, and deposition on plastic substrates.
- Chapter 6 deals with the fabrication and characterization of transparent ZnO-based thin film transistors. It discusses the problems encountered in the fabrication of a TFT, and the steps taken to rectify the situation.
- Chapter 7 provides the conclusions and recommendations for future work.

Chapter 2

Literature Review and Technical Background

2.1 Transparent Conducting Metal Oxides

There are at least two types of transparent conducting films: thin metal films and conducting oxide films such as indium tin oxide (ITO) and ZnO. These films are of great importance for IR reflective glass windows, touch-screens, flat panel display, solar cells, and electrochromic devices. The oxide films usually show a very high transmission in the visible region, but reflect in the infrared. The first report of such a material (CdO) appears to have been made by Badeker in 1907. [14] A number of additional transparent conducting oxides (TCOs), such as ZnO, In_2O_3, and SnO_2, have been known to exist for many years.

ZnO is a possible less expensive replacement for ITO (indium tin oxide), as indium is a relatively expensive raw material.

The simultaneous existence of optical transparency and electrical conductivity requires a wide bandgap (~>3eV) material, doped (intentionally or unintentionally) so as to modulate the Fermi level close enough to the conduction (valence) band to induce mobile electrons (holes).[15] Due to the relatively low mobilities exhibited by this class of

materials, typical transparent conductors used in passive applications are degenerately doped in order to maximize their conductivity.

Until recently, all known transparent conductors were n-type. The first report of p-type conductivity in a transparent material ($CuAlO_2$) came in 1997. [16] Since this report, a number of new p-type as well as n-type transparent conducting materials have been discovered. Note that the division of transparent conducting materials by conductivity type is quite reasonable, in that bipolar conductivity in this class of materials is exceedingly rare. To date only two transparent semiconductors, GaN [17] and $CuInO_2$ [18], have been reported to exhibit bipolar conductivity.

In our case, we are only interested in n-type conducting oxides as our focus is on ZnO. Table 2.1 shows the resistivity and transmittance of n-type conducting oxides deposited by various methods, under their respective optimal temperatures.

Table 2.1: Comparison of transparent conducting oxide prepared by various deposition methods

Deposition method	FCVA	Sputtering[19]	Sputtering[20]	FCVA	Sputtering[21]	Excimer laser ablation[22]
	ZnO	ZnO	ITO	ZnO:Al	ZnO:Al	ZnO:Ga
ρ (Ωcm)	$3x10^{-3}$	$3x10^{-3}$	$3x10^{-4}$	$1x10^{-4}$	$7x10^{-4}$	$2.7x10^{-4}$
Transmittance (%)	90	80	>80	90	85	90
Substrate Temperature (°C)	150	150	NA	80	150	300

A widely reported method of increasing the conductivity of ZnO is to dope it with aluminum. H. Kim [23] reported on single crystal ZnO:Al films deposited on sapphire substrates by pulsed laser deposition, with substrate temperatures ranging from 25 to 680°C. They achieved a lowest resistivity of 2.2×10^{-4} Ωcm, and the average transmission in the visible spectrum was 90%. As their ZnO:Al are single crystal films, the low resistivity is mainly attributed to a high carrier mobility, due to less grain boundary scattering in single crystal films.

M. Chen [55] reported on transparent conductive oxide ZnO:Al films prepared by dc magnetron reactive sputtering. The visible transmittance of above 80% and infrared reflectance of above 80% were obtained. The minimum resistivity is 4.2×10^{-4} Ωcm with the carrier concentration of 9.21×10^{20} cm^{-3} and Hall mobility of 16.0 cm^2 V^{-1} s^{-1}. These values of resistivity are comparable with that of the ZnO:Al films deposited by FCVA.

2.2 TFT Background/Introduction

2.2.1 Introduction to TFTs

Thin film transistor has been around for quite some time, and it has found itself in many applications in the world today. The dominant ones today are active matrix liquid crystal displays (AMLCDs) used in flat panel display. Vast majority of today's flat panel displays are AMLCDs, which is made primarily of amorphous silicon. Enormous experimental research and theoretical calculations have been performed on poly-Si based TFTs, and its activity in TFTs performance were reported. Some of the drawbacks of amorphous silicon are that it is opaque and light sensitive, which require light shielding. Being opaque affects its performance, as it is linked to the transmittivity of the LCD.

Very recently ZnO-based thin film transistors (TFT) have been reported, due to its strong potential in replacing amorphous silicon as the channel layer. There are also some works on thin film transistors made of transparent channel semiconductors (ZnO). Transparent electronics is catching up in the AMLCDs industry due to its obvious advantage in allowing more light through each pixel, yielding a brighter, more efficient display. Furthermore, this leads to a reduction of power consumption.

The most common types of TFTs in use today are: (a) hydrogenated amorphous silicon TFTs, (b) polysilicon TFTs, and (c) organic-based TFTs.

Hydrogenated amorphous silicon

Silicon is normally tetrahedral bonded to four neighboring silicon atoms. This is also the case in amorphous silicon; however, it does not form a continuous crystalline lattice as in crystalline silicon. Some atoms may actually have dangling bonds, which occur when it does not bond to four neighboring atoms. Since not all the atoms are four-fold coordinated, amorphous silicon is said to be under-coordinated. These dangling bonds are defects in the continuous random network, which can be improved by introducing hydrogen into the silicon. It then becomes hydrogenated amorphous silicon.

Polycrystalline silicon

Polysilicon TFT refers to TFT constructed using polycrystalline silicon.

Depending upon the technology used to fabricate TFTs, we distinguish between amorphous-Si TFTs (a-Si TFTs) and poly-Si TFTs. [24] Poly-Si technology presents advantages over a-Si technology on the achievable size-versus-resolution limits for the display, as well as the opportunity to monolithically integrate additional functionality on the panel (i.e., beyond the pixel matrix). The advantages of poly-Si technology stem primarily from the significant performance gains of poly-Si TFTs over a-Si TFTs.

Unlike MOSFETs, where the device active layer is part of the substrate, in the case of TFTs the active layer needs to be separately formed on the host substrate. The common way of doing that, for poly-Si TFTs, is by deposition of an amorphous Si film on the host

substrate and the subsequent transformation of the a-Si film to poly-Si by means of an appropriate annealing step.

Organic semiconductor

TFTs have also been fabricated using organic semiconductors. Organic semiconductors have been studied since the early 1950s, dealing essentially with small molecules, e.g. condensed hydro-carbons and dyes. However, their semiconducting characteristics were poor and their reproducibility was very low, which made these ill-defined materials incompatible with any real device development.

Answers came in 1990, when it was shown that relatively short conjugated oligomers, e.g., sexithiophene, showed a mobility of the order of 10^{-1} $cm^2V^{-1}s^{-1}$, almost matching that of a-Si:H. [25] This result, together with the simultaneous first demonstration of a light-emitting diode fabricated from PPV (polyphenylenevinylene), marked the birth of very intensive work on organic-based devices, in both university and private-sector laboratories, which led to a blossoming of organic-based devices.

The most reliable and higher mobility organic TFTs were achieved using small molecule materials like pentacene. Pentacene, a small molecule aromatic hydrocarbon comprised of five linearly fused benzene rings, has been used to fabricate thin film transistors (TFTs) with performance comparable to devices using hydrogenated amorphous silicon; such devices are of interest for use in displays and other broad area electronic applications. [26]

2.2.2 Transparent TFTs

The first report on a semi-transparent thin film transistor (TFT) appeared in 1996, wherein Prins *et al.* reported the fabrication of a transparent ferroelectric thin film transistor. [27, 28] SnO_2 : Sb is used for the channel material, $SrRuO_3$ for the gate electrode, and $PbZr_{0.2}Ti_{0.8}O_3$ (PZT) for the gate insulator. PZT, a well-known ferroelectric material, is polarized by the application of a voltage to the gate electrode, thus allowing the transistor to be used as a memory element. However, the transparency for this TFT was rather low, and the authors stated optical absorption is some tens of percents, without furnishing any specific data.

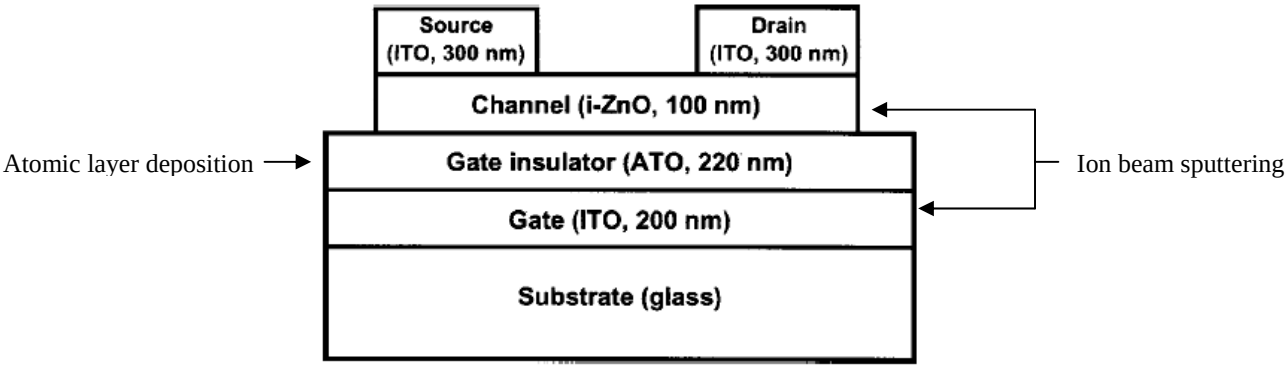

Figure 2.1 TFT by R. L. Hoffman

R. L. Hoffman *et al.* reported on ZnO-based transparent thin-film transistors, with the channel layer deposited by ion beam sputtering, in August 2002. [29] Figure 2.1 shows the structure of the TFT fabricated by Hoffman. Highly transparent ZnO-based TFTs were fabricated with optical transmission (including substrate) of ~75% in the visible portion of the electromagnetic spectrum. Current-voltage measurements indicate n-channel,

enhancement-mode TFT operation with excellent drain current saturation and a drain current on-to-off ratio of ~10^7. Threshold voltages and channel mobilities of devices fabricated to date range from ~10 to 20 V and ~0.3 to 2.5 cm^2/Vs, respectively. Exposure to ambient light has little to no observable effect on the drain current. In contrast, exposure to intense ultraviolet radiation results in persistent photoconductivity, associated with the creation of electron-hole pairs by ultraviolet photons with energies greater than the ZnO band gap. Light sensitivity is reduced by decreasing the ZnO channel layer thickness.

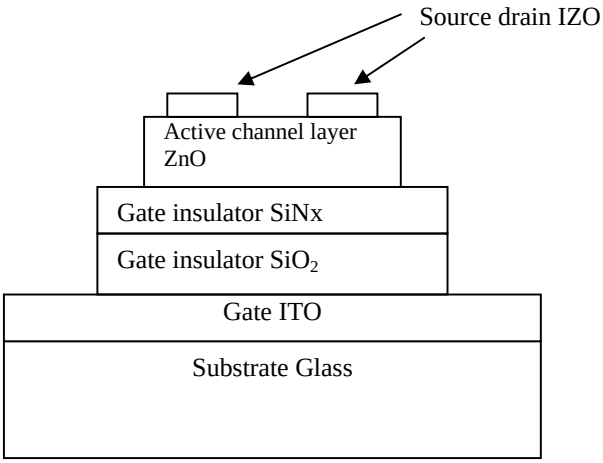

Figure 2.2 TFT by S. Masuda

Satoshi Masuda *et al.* used pulsed laser deposition to fabricate the ZnO active layer in several TFTs, some transparent and others opaque. [30] Figure 2.2 shows the structure of the transparent ZnO-based TFT fabricated by S. Masuda. The opaque TFTs were fabricated on Si substrates, while the transparent TFTs were fabricated on glass coated with indium tin oxide (ITO), with the ITO acting as the gate. They used the bottom gate structure for their TFTs. The ZnO layers were deposited using pulsed laser deposition at

450°C at an oxygen pressure of 3 mTorr, and the material that was formed had a background carrier concentration of less than $5x10^{16}$ cm^{-3}. A double layer gate insulator consisting of SiO_2 and SiN_x was effective in suppressing leakage current and enabling the ZnO-TFT to operate successfully. The I_{on}/I_{off} ratio of ZnO-TFTs fabricated on Si wafers was more than 10^5 and the optical transmittance of ZnO-TFTs fabricated on glass was more than 80%. These results show that it is possible to fabricate a transparent TFT that can even be operated in the presence of visible light.

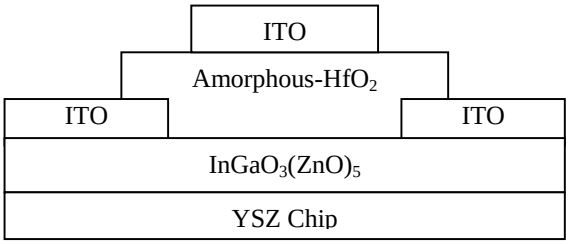

Figure 2.3 TFT by K. Nomura

K. Nomura *et al.* fabricated a ZnO-based TFT with the structure as shown in Figure 2.3. [31] A top-gate TFT was fabricated with the use of a single-crystalline film grown on a 10mm by 10mm YSZ chip. The source, drain, gate contacts, and gate insulator were defined by standard photolithography and lift-off techniques. An 80nm thick amorphous hafnium oxide (a-HfO_2) layer was used for the gate insulator, and while ITO was used for source, drain, and gate electrodes. For the ITO and a-HfO_2 layers were deposited by Pulsed Laser Deposition (PLD) at room temperature. The dielectric constant of a-HfO_2 films was measured to be 18, with the channel length and gate width of 50μm and 200μm, respectively, corresponding to a width-to-length ratio of 4:1. The chip is optically transparent in the whole visible-light region. The optical transmittance is 80% in the

wavelength range between 390 nm and 3200 nm, which indicates that transmission losses due to the film and the TFTs are negligible.

2.2.3 Comparison of TFTs fabricated by three different teams

Source, drain and gate

With regards to the source, drain and gates of the thin film transistors, there was marginal difference in the types that were used. ITO was primarily used for all the three projects that were covered.

Insulating layer

Variations of FET technology are based on different ways of generating the electric field.

As depicted earlier in the sections, the following were some of the metal oxide that were used for the insulating layers

1. 220 nm thick layer of aluminum–titanium oxide ATO

   Technique: Atomic layer deposition
2. Double insulating layer, comprising of 50nm of SiN_x on top of 250nm SiO_2

   Technique: Plasma CVD
3. 80nm thick amorphous HfO_2

   Technique: PLD at room temperature

Active channel layer:

Table 2.2 sums up the fabrication technique used and also the dimension of the ZnO active channel layer. These are important parameters that affect the performance of a transistor.

Table 2.2: Summary of fabrication method and dimension of ZnO

	Technique used to grow active channel	Thickness (nm)	Channel width (μm)	Channel length (μm)
R. L. Hoffman	Ion beam sputtering	100	15000	1500
S. Masuda	PLD	140	3500	50
K. Nomura	PLD	120	200	50

Some of the performance characterization parameters include, charge mobility, transmittivity, I_{on}/I_{off}, and V_{th}. Table 2.3 summaries the performance of the three research work previously done.

The choice of a gate insulator material is also important factor in achieving good performance results. For K. Nomura's work, where amorphous hafnium oxide was used for the gate insulator, the channel mobility was 80 cm^2/Vs.

Table 2.3: Performance summary of the different thin film transistors

	Channel mobility (cm^2/Vs)	V_{th} (V)	I_{on}/I_{off}	Average optical transmission
R. L. Hoffman	0.35-0.45	10-15	10^7	75%
S. Masuda	-	2.5	10^5	>80%
K. Nomura	80	3	10^6	>80%

Most of the field effect electron mobility of ZnO based TFT reported are in the range of 0.01-3cm^2/Vs, while their on/off current ratio ranges from 10^2 to 10^7. So what was achieved by K. Nomura (80 cm^2/Vs) provided a significant step forward in the next generation of optoelectronics. This improvement in performance is because single crystalline oxide was fabricated. However because of the complex structure and composition, it is difficult to obtain single-crystalline films of such oxides with the use of a conventional vapor-phase growth technique alone. That usually requires a high temperature to grow in single crystalline phase.

In this thesis however, fabrication is done in a low temperature condition. Because deposition on a plastic substrate would be the future goal, so this report concentrates on searching for the appropriate fabrication condition in a low temperature context.

2.3 Filtered Cathodic Vacuum Arc Technique

2.3.1 Characteristics of FCVA

In cathodic arc deposition [32], the consumable cathode is transferred to the plasma state at microscopic, non-stationary cathode spots—locations of extremely high current density, power density, and plasma density. [33] The plasma expanding from cathode spots contains ions that are usually multiply charged and have a kinetic energy in the range 18 to 150 eV, depending on the cathode material (Table 2.4 [32]). The higher the cohesive energy of the solid cathode, the greater are the arc burning voltage, power density, average ion charge state, electron temperature, and ion kinetic energy (cohesive energy rule [34]). Cathodic arc plasma deposition is perhaps the oldest technique of energetic deposition.

Due to the explosive nature of plasma formation, cathodic arc processes also produce unwanted droplets and debris particles in the μm and sub-μm range, commonly referred to as macroparticles.

The cathodic vacuum arc has been recognized as a cost-effective method of producing thin film coatings.[35] One important advantage of the cathodic vacuum arc process is the formation of a copious quantity of ions of the cathode materials. This is in contrast to other Physical Vapor Deposition (PVD) techniques such as magnetron sputtering and electron beam evaporation where the depositing species forming the coating are primarily neutral atoms. As such, the charged particles produced by the cathodic vacuum arc process can be controlled both with respect to the path taken from the cathode arc source

Table 2.4: Cohesive energy, displacement energy, burning voltage at 300A, kinetic energies for various cathodic arc plasmas

Cathode material	Cohesive energy (eV/atom)	Displ. Energy (eV)	Arc burning voltage (V)	Kinetic ion energy (eV)
Li	1.63	N.A.	23.5	19
C (graphite)	7.37	25	29.6	19
Mg	1.51	10	18.8	49
Al	3.39	16	23.6	33
Si	4.63	13	27.5	34
Ti	4.85	19	21.3	59
V	5.31	26	22.5	70
Cr	4.1	28	22.9	71
Fe	4.28	17	22.7	46
Co	4.39	22	22.8	44
Ni	4.44	23	20.5	41
Cu	3.49	19	23.4	57
Zn	1.35	14	15.5	36
Ge	3.85	15	17.5	45
Y	4.37	N.A.	18.1	80

to the coating substrate, and the kinetic energy with which they strike the substrate. However, the cathodic arcs normally generate undesirable macroparticles, which end up as defects in the coatings.

Macroparticle [36] contamination of the cathodic arc plasma is for most applications a disadvantage and for some a fatal defect. Most tribological and decorative applications would be better served by a macroparticle-reduced process, while others, including particularly most applications to the semiconductor and magnetic storage industries, call for essentially macroparticle-free film deposition. There is incentive for improved theoretical models and for the development of new macro-filtering schemes. Much progress has been made, and a number of new systems and approaches have been discovered.

The approach to macroparticle filtering that has seen the most significant progress is the use of curved magnetic guide fields, first introduced by Aksenov and coworkers in the 1970s. [37, 38, 39] Plasma from the cathodic arc source is injected into a bent solenoidal magnetic field region, a quarter-torus being typical, where the plasma stream is bent through an angle of 90°. The plasma is transported through the duct, with some loss, while the macroparticles are not magnetically guided and are lost from the plasma stream. The goal of duct research is thus to increase the plasma transport efficiency through the duct and to reduce the residual macroparticle flux at the substrate location.

A detailed experimental investigation of duct plasma transport as a function of duct parameters was made by Anders and coworkers. [40, 41, 42] The importance of the flow of magnetized electrons in determining the transport of unmagnetized ions via ambipolar electric fields was pointed out. For good plasma transport the duct must be biased with

respect to the plasma, typically by about +10 to +20V, an effect noted in the pioneering work of Aksenov and coworkers. This feature was recognized also by Bilek and coworkers who showed that a similar effect can be produced by applying a positive bias to a strip electrode that is located near the outer wall of the interior of the duct. These kinds of optimized 90° ducts can achieve a plasma transport efficiency of up to about 25%.

Anders has taken the concept further in the S-duct. [43] Here the macroparticle transport is reduced to an unmeasurably low level by the use of two 90° ducts in series, but done in such a way as to offset the curvature drift [44, 45] of the metal plasma stream toward the duct wall. The plasma transport efficiency is also reduced to about 6% for optimum operation. This draconian solution to macroparticle removal is suited to those applications where essentially no macroparticles can be tolerated and the required film thickness is small; the suitability of the approach for producing very thin, macroparticle-free, diamond-like carbon protective overcoats for magnetic storage disks has been demonstrated.[46, 47]

Somewhat offsetting the disadvantage of low plasma transport efficiency are the results of Schulke and coworkers, who investigated the transport of high current arc plasmas through a 90° duct. [48] The peak arc current was up to several kiloamperes, and the plasma ion current at the filter exit was as much as 7% of the arc current, for a duct transport efficiency (ratio of ion current at duct exit to that at duct entrance) of up to 35%. Extrapolation of this result to an S-duct configuration would predict usable S-duct-filtered ion current in the tens of amperes range. These impressively large plasma currents could find industrial application.

Aksenov and coworkers have described a novel kind of geometry involving an axially symmetric magnetic filter configuration. Both mirror and ring-cusp magnetic geometries (adding and opposing magnetic field coils, respectively) were investigated. Good efficiency and high film deposition rates were demonstrated (10 μm h^{-1} of TiN over 0.2 m^2 substrate area).

Recently an in-line magnetic filter system has been described by Ryabchikov and coworkers. [49, 50] In this configuration a concentric, circular, "venetian blind" arrangement (a nested set of tapered sections) is used. A reduction of two orders of magnitude in the macroparticle fraction and a plasma transport efficiency of up to 70% were reported. This kind of system could be nicely suited to large facilities.

FCVA is a variant of the techniques mentioned above, employing an off-plane double bend instead of the S-duct.

FCVA has been used in the deposition of tetrahedral amorphous carbon (ta-C) films. Clean ta-C films can be deposited at room temperature. The amorphous tetrahedral (sp^3) bonding can be as high as 87%, where the high sp^3 content in the film results in extreme hardness (~70 GPa), thermal stability, high electrical resistivity, wide optical band gap (~2.5eV), smooth surface and low friction, and transparency in wide spectral range.

The near-100% ionization of the cathode material in the plasma means that the impact energy of the depositing ions at the growth surface can be readily controlled using electric fields. Their high-energy plasma plume will readily ionize most background gases. These features make FCVA an ideal source for the production of metal oxides ad nitrides. [51]

Apart from the abovementioned features, the FCVA technique also has the following advantages:

a. The energetic bombardment of the growing film by the incoming ions produces dense and adherent films virtually free of voids.

b. With the employment of the double bend technology, the film is virtually macroparticle free.

c. During the deposition, some parameters like substrate temperature can be independently controlled for there is no direct heat transfer from the source area to the substrate.

d. The system can coat a large area uniformly with a carefully designed scanning control.

2.3.2 FCVA Deposition System

Figure 2.4 shows the schematic of the filtered cathodic vacuum arc deposition apparatus.

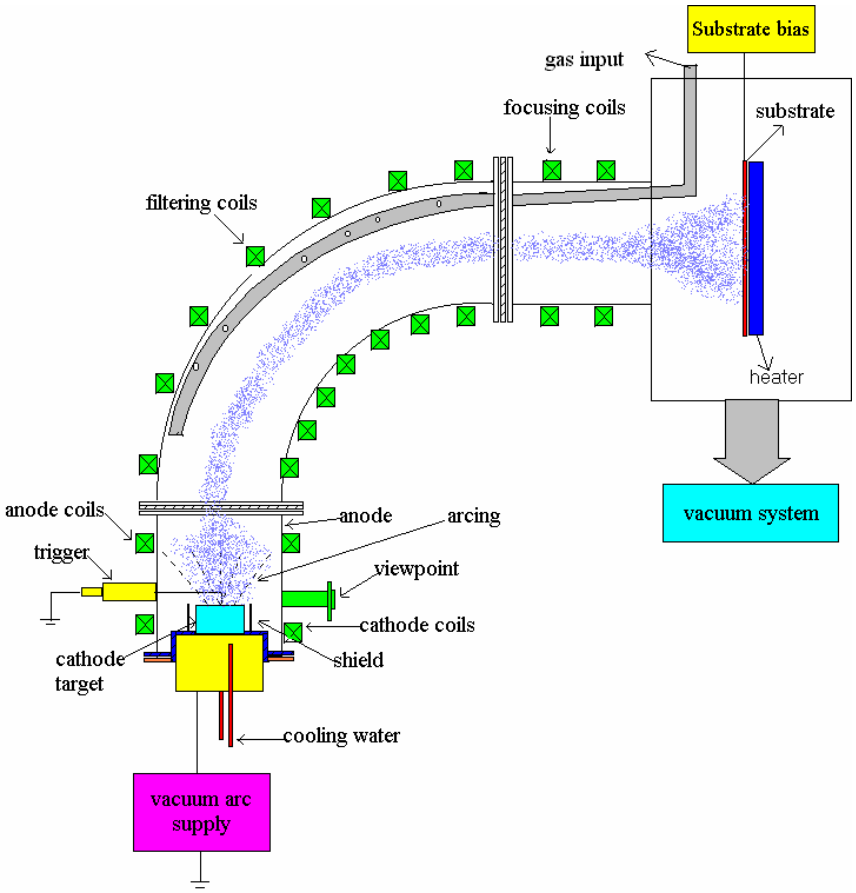

Figure 2.4 Filtered cathodic vacuum arc deposition system

The system includes a cathodic arc source, plasma filtering duct and a deposition chamber. [35] The cathodic vacuum arc source consists of five parts: the power supply, arc trigger, target material (cathode), water-cooled target holder and magnetic coil for controlling the motion of the cathode spots. The power supply used is an electric welding machine (Prestotig 250) with a current range from 10 to 250 A. The anode is grounded (connected to deposition chamber) and the cathode is connected to the target source. The

arc trigger is also grounded to initiate an arc jet like in the welding. Plasma forms in a vacuum arc discharge between the gap of cathode and the grounded anode.

The system was evacuated to below 10^{-5} Torr. The arc can be ignited by allowing the arc trigger to come into contact with the cathode surface, and quickly retrieving the trigger to open the circuit. After this ignition process, the arc can be self-sustained. In the apparatus, the cathode target source has a diameter of 60 mm, and is mounted onto a stainless steel water-cooled holder.

The toroidal solenoid is a stainless steel, off-plane double bend duct with the copper coil wound externally, tightly hugging the surface of the bend. The magnetic fields can be adjusted to a maximum of 45 mT by supplying a current of 25A to the coil. A removable metallic baffle, acting as a mechanical barrier, was also installed inside the duct to filter the unwanted macroparticles. The off-plane double bend filter was insulated from the anode and the chamber, which can be floating or biased to a positive voltage when the plasma is passing through it.

The deposition chamber is placed at the exit of the filter. In between, there is a straight section wound with copper coil producing magnetic field to focus the plasma flux.

Chapter 3

Fabrication

3.1 Deposition Parameters

Zinc with purity of 99.9% was used as the target. High purity (99.99%) O_2 gas was used as the reactant gas. An arc current of 60A was used to generate the plasma and the typical base pressure was 2×10^{-6} Torr. The substrate temperature was monitored by a thermocouple attached to the substrate surface. A toroidal magnetic field of approximately 40 mT was employed to produce the axial and curvilinear fields to steer the plasma. The substrates used were (100) *p*-type silicon wafers with a thickness of 400±25 μm, and quartz glass.

For the experiments performed to investigate the influence of negative substrate bias on the films, the substrate temperature was maintained at 260°C, the oxygen pressure was kept at 9×10^{-5} Torr, and the substrate bias was varied from –10 to –200V. For the experiments performed to investigate the influence of temperature on the films, the oxygen pressure was kept at 9×10^{-5} Torr, the substrate was left floating, and the temperature was varied from 100 to 420°C. For the experiments performed to investigate the influence of the oxygen pressure on the films, the substrate temperature was

maintained at 260°C, the substrate was left floating, and the oxygen pressure was varied from 3.8×10^{-5} to 3.4×10^{-4} Torr.

In the case of ZnO:Al thin film preparation, typical working pressure was 5×10^{-4} Torr, and substrate temperature was in the range of room temperature to 350°C. A Zn target with 5 at.% (atomic percentage) of Al was used for the samples prepared to investigate the effect of varying substrate temperatures. To study the effect of varying Al content, targets with Al content of 1, 2, 3, 5 and 7 at.% were used. The substrates used were quartz glass and silicon (100) wafer.

3.2 Deposition On Plastic Substrates

As polymer substrates cannot withstand high temperatures, for films deposited on polymer substrates, the substrate temperature used was room temperature. The working pressure was in the range 3×10^{-4} to 1×10^{-3} Torr. The substrates used were polyethylene naphthalate (PEN).

3.3 Macroparticle-free Films

In the current project, an off-plane double bend duct for magnetic field is used for macroparticle filtering. The ZnO films prepared by our team are macroparticle-free, as can be seen from the SEM micrograph in Figure 3.1.

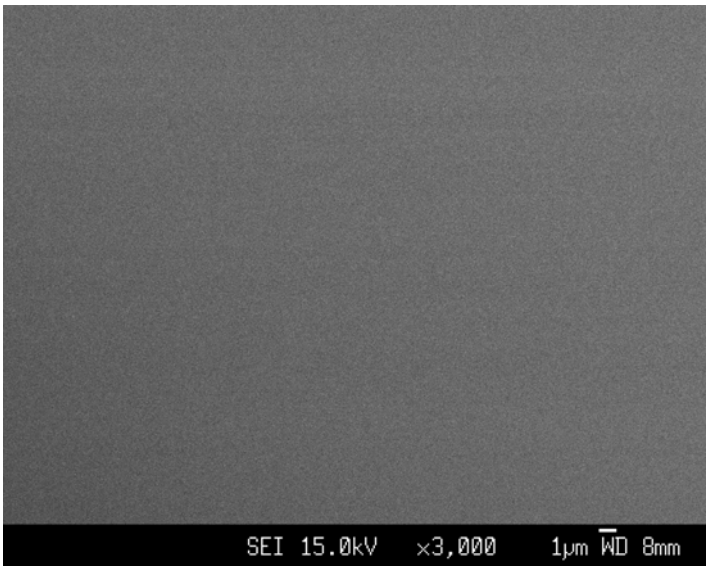

Figure 3.1 SEM micrograph of ZnO film deposited by FCVA technique

3.4 Growth Rate

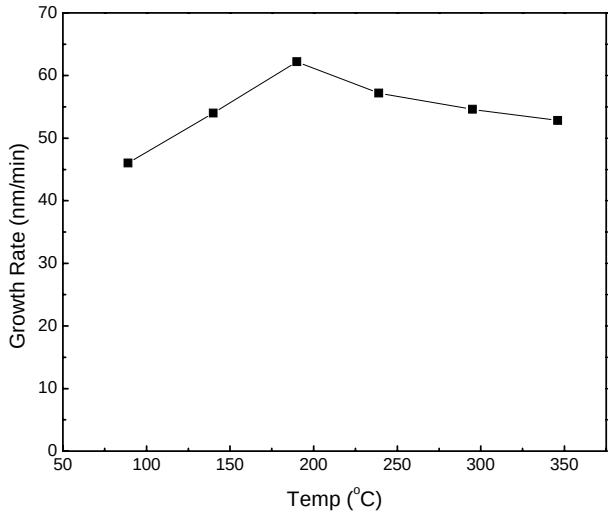

Figure 3.2 Variation of growth rate with deposition temperature

Figure 3.2 shows the influence of deposition temperature on growth rate, with a constant pressure of 6×10^{-4} Torr. At higher temperatures, the growth rate is lower as thermal energy imparted to zinc atoms reaching the substrate creates a sort of sputtering effect, causing zinc atoms to be expelled from the surface of the film. On the other hand, for films grown at temperatures below 190°C, growth rate increases with increase in temperature. This is so as the oxygen atoms will, as temperature is increased, react more readily with zinc atoms in forming crystalline grains.

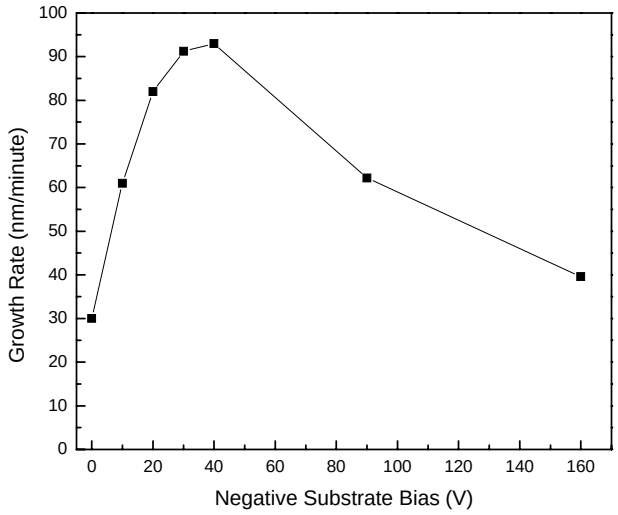

Figure 3.3 Variation of growth rate with negative substrate bias

Figure 3.3 shows the dependence of growth rate on negative substrate bias. The kinetic energy of zinc ions from the plasma increases with increase in negative bias. For films deposited with bias of less than 40V, the increase in kinetic energy of zinc ions results in more rapid formation of ZnO crystallites, the growth rate thus increased with increase in bias. As negative bias was increased beyond 40V, the growth rate decreased with increase in bias, because the bombardment of the film surface by energetic zinc ions produces a sputtering effect.

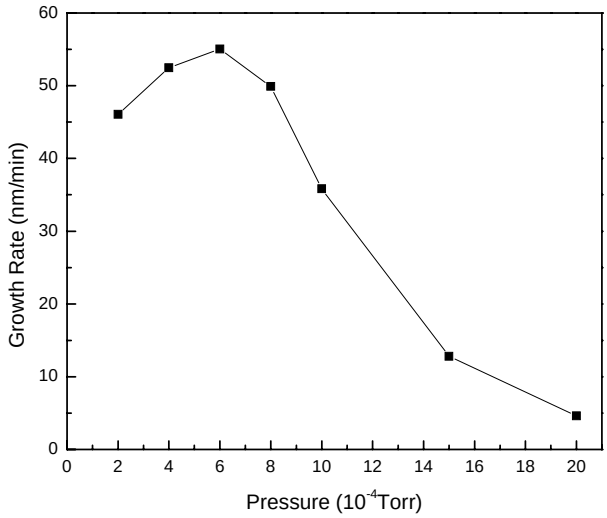

Figure 3.4 Influence of pressure on growth rate at deposition temperature of 250℃

Figure 3.4 shows the influence of pressure on growth rate at deposition temperature of 250°C. The growth rate initially increased with increase in pressure as more oxygen was introduced, promoting faster formation of ZnO crystalline grains. However, as pressure was increased further, the growth rate decreased because the plasma was weakened by its increased collisions with oxygen atoms, so that less zinc ions reached the surface of the substrate.

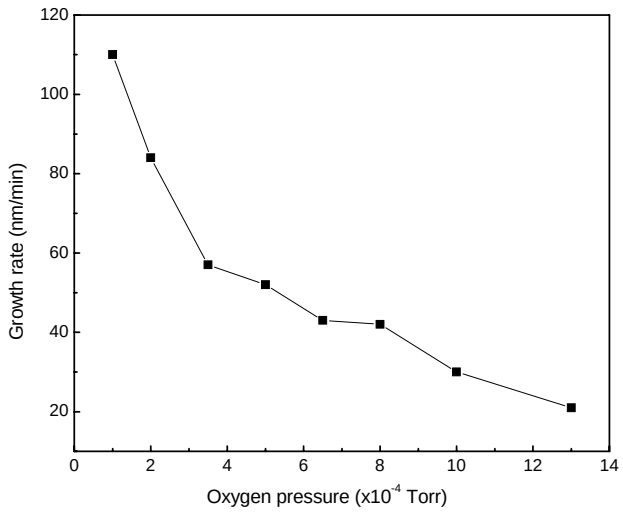

Figure 3.5 Influence of pressure on growth rate for films deposited at room temperature

Figure 3.5 shows the influence of pressure on growth rate for the films deposited at room temperature. Unlike the case for the set of data for deposition temperature of 250°C, the growth rate at lower pressures did not increase with increasing pressure. This is because at room temperature, the deficiency in oxygen due to low pressure does not inhibit growth of ZnO films while it does for high deposition temperatures. Instead of inhibiting film growth, the deficiency in oxygen merely results in zinc-rich films. This mechanism operates only at low temperatures as, at high temperatures, thermal energy imparted to zinc atoms reaching the substrate creates a sort of sputtering effect, causing zinc atoms to be expelled from the surface of the film.

Chapter 4

Characterization Techniques

4.1 Atomic Force Microscope

The surface morphology of the films was investigated by AFM in the tapping mode (Dimension 3000 scanning probe microscope from Digital Instruments). The Dimension^{TM} 3000 consists of a rigid stage mounted on a granite block, and features a beam deflection SPM head and integral, on-axis video microscope. The system is ideally suited to imaging large, unbroken samples such as integrated circuit wafers or data storage disk media. Figure 4.1 shows the Dimension 3000 SPM. The Dimension 3000 produces high-resolution, three-dimensional images by scanning a sharp probe over the sample surface. The probe is part of a flexible cantilever, which is mounted on one end of a cylindrical piezoelectric tube. The piezo tube is rigidly mounted near the top of the microscope. Voltages applied to the X and Y electrodes on the piezoelectric tube deflect the tube horizontally to produce a precise raster scan over the sample surface.

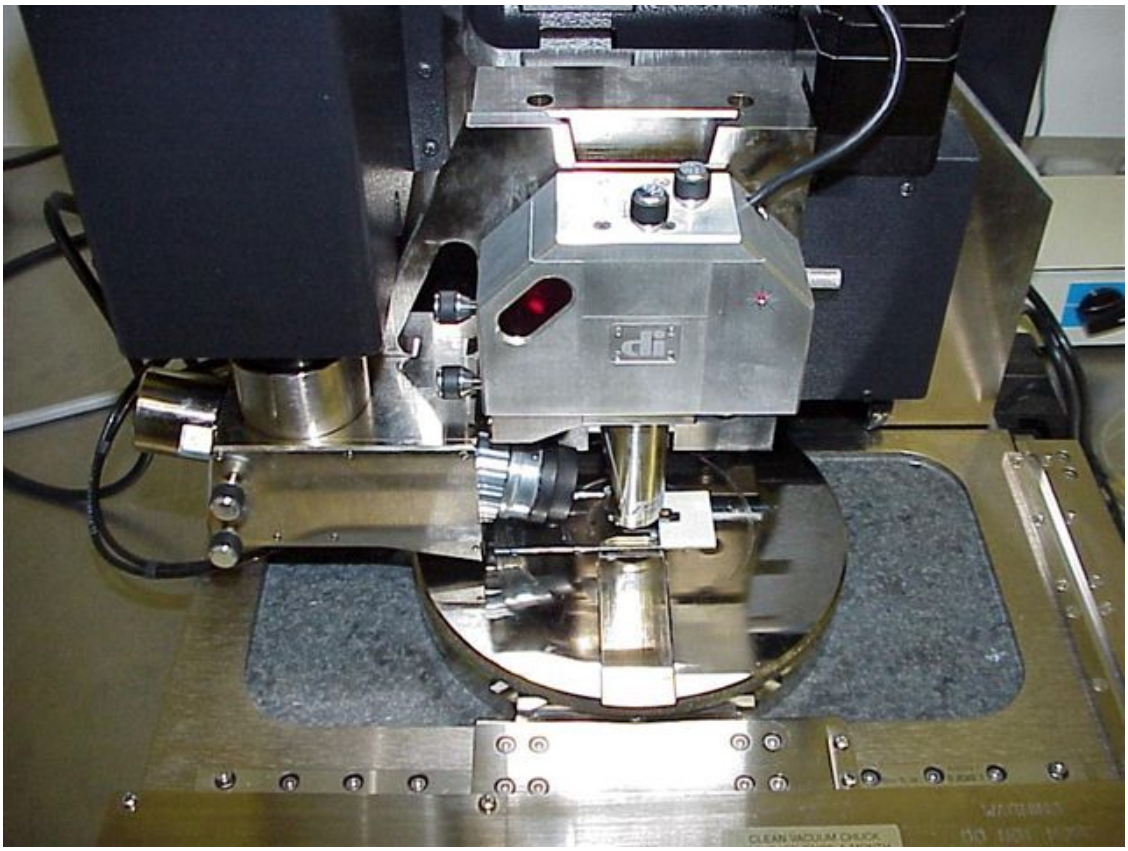

Figure 4.1 Dimension 3000 Scanning Probe Microscope.

The vertical height of the probe controlled by a voltage applied to the Z electrode on the piezo tube. A stepper motor coupled to a lead screw translates a crossed roller slide to which the sample is attached. A separate motor drive allows the height of the microscope and probe to be adjusted relative to the sample surface. The Dimension 3000's motorized Z-stage provides accurate, automatic tip engagement and approach.

Basic Principle of Tapping Mode

First consider a cantilever oscillating in free air at its resonant frequency. A piezo stack excites the cantilever's substrate vertically, causing the tip to bounce up and down. As the

cantilever bounces vertically, the reflected laser beam is deflected in a regular pattern over a photodiode array, generating a sinusoidal, electronic signal.

Now consider the same cantilever at the sample surface, as illustrated by Figure 4.2. Although the piezo stack continues to excite the cantilever's substrate with the same energy, the tip is deflected in its encounter with the surface. The reflected laser beam (return signal) reveals information about the vertical height of the sample surface and some characteristics of the sample material itself. These material characteristics may include elasticity (hardness), magnetic and/or electric forces present.

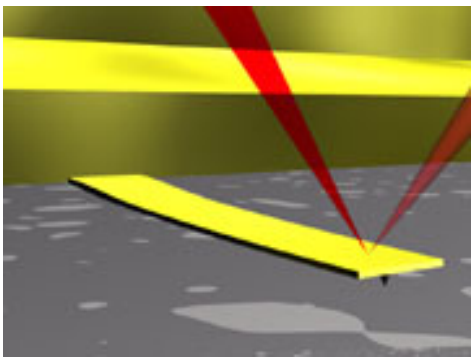

Figure 4.2 Cantilever in tapping mode.

4.2 Hall Effect

The resistivity, carrier concentration and Hall mobility were measured by standard van der Pauw configuration at room temperature (EGK HEM2000). The HEM2000 Hall effect measurement system is a complete system for measuring the resistivity, carrier concentration, and mobility of semiconductors. The system can be used to characterize various materials including silicon and compound semiconductors at room temperature.

Characteristics

Compact Desktop Model - Permanent magnets and a small circuit system are used instead of an electric magnet system and a bulky constant current source, producing a compact, desktop design.

Simplicity and Accuracy

Five stage current ranges reduce the allowance error to a minimum. A ten turn current adjustment knob produces precise result.

Simple Operation - Speedy Data Results

Data is input by a simple operation providing bulk/sheet carrier concentration, mobility, Hall coefficient, bulk resistivity, conductivity, magnetoresistance, and alpha (Vertical/Horizontal ratio of resistance).

Equipment Composition

- Constant current source supply system
- Sample measurement case
- Permanent magnet set
- Hall Effect Measurement Program (Windows)

4.3 Scanning Electron Microscope

The cross-sectional microstructure of the films was studied by a field emission scanning electron microscope (SEM) (JEOL-6340F) on cleaved samples, with the SEM operated at 15 keV.

The scanning electron microscope (SEM) has unique capabilities for analyzing surfaces. It is analogous to the reflected light microscope, although different radiation sources serve to produce the required illumination. [52] Whereas the reflected light microscope forms an image from light reflected from a sample surface, the SEM uses electrons for image formation. The different wavelengths of these radiation sources result in different resolution levels: electrons have a much shorter wavelength than light photons, and shorter wavelengths are capable of generating high-resolution information. Enhanced resolution in turn permits higher magnification without loss of detail. The maximum magnification of the light microscope is about 2000×; beyond this level is “empty magnification,” or the point where increased magnification does not provide additional information. This upper magnification limit is a function of the wavelength of visible light, 2000 Å, which equals the theoretical maximum resolution of conventional light microscopes. In comparison, the wavelength of electrons is less than 0.5 Å, and theoretically the maximum magnification of electron beam instruments is beyond 800,000×. Because of instrumental parameters, practical magnification and resolution limits are ~75,000× and 40 Å in a conventional SEM.

Another difference between light and scanning electron imaging concerns the *depth of field*, defined as the ability to maintain focus across a field of view regardless of surface

roughness. Human binocular vision permits observation and interpretation of depth of field in three-dimensional objects. Conventional photographs and photomicrographs are two-dimensional representations; the dimension of depth is suppressed when recording an image with a diffuse light source. In contrast, SEM micrographs maintain the three-dimensional appearance of textured surfaces, a phenomenon due to the high depth of field of scanning instruments. Depth of field is further suppressed in both macro-photography and photomicrography as magnification is increased. At 10×, the relative depth of field of a light microscope is about 250 μm, while that of the SEM is about 1000 μm; at 1200× the depth of field of a light microscope is ~0.08 μm; at 10,000×, the depth of field of the SEM is 10 μm. Thus, photographers are often challenged to record rough surfaces while maintaining depth of field (through determination of the "optimal aperture"); scanning electron microscopists readily record smooth or rough surfaces.

The combination of high resolution, an extensive magnification range, and high depth of field makes the SEM uniquely suited for the study of surfaces. As such, it is an indispensable tool in materials science research and development.

4.4 X-ray Diffractometer

X-ray diffraction was performed using SHIMADZU (XRD-6000) X-ray diffractometer. The diffraction was excited by Cu K_α radiation (wavelength at 1.54 angstrom) at 50 kV and 20mA. The scans were performed in Bragg-Bretano ($\theta/2\theta$) geometry, and the scanning range was between $2\theta = 30°$ and 65°.

The x-ray incident on the sample is ideally monochromatic. For that purpose, the beam to be monochromatized is incident on a monochromator. A monochromator is either a single crystal or a highly oriented polycrystalline material, which allows a diffracted beam at a well-defined monochromatic wavelength to emanate from it according to Bragg's law. For less stringent monochromatization, a filter is used; the filter is a material that preferentially absorbs radiation of wavelength below a certain value, which is called the absorption edge, in order to remove the K_β radiation.

The Shimadzu XRD-6000 consists of the following parts:

(1) X-ray tube

It receives high voltage and cooling water from the x-ray tube shield to generate x-rays.

(2) X-ray tube shield

This tube shield holds the x-ray tube. It supplies the power and cooling water. It also cuts off x-rays harmful to analysis.

(3) Goniometer

X-rays diffracted on a sample are measured accurately with the x-ray spectrometer. According to analytical techniques, the x-ray optical systems can be changed.

(4) Scintillation detector

X-ray detector through the use of the x-ray scintillation of a solid body. For the luminous body, NaI single crystal activated with a trace quantity of Tl is used.

Principle of operation

For the X-ray diffractometer, x-rays emitted from the x-ray tube undergo the limitation of the divergence slit and hit a sample loaded in the center of the goniometer. The x-rays diffracted from the sample converge on the receiving slit, which is located in a position symmetrical with respect to the x-ray focus of the x-ray tube, viewed from the sample. These x-rays are captured by the scintillation detector and converted into electric signals. The signals from the scintillation detector, after the elimination of noise components, are counted by the pulse height analyzer (PHA).

The x-ray intensity is expressed in the magnitude of a counted value. The distance between atomic planes where x-rays are diffracted can be obtained from the Bragg condition below,

$$2d \sin\theta = n\lambda$$

where θ = Peak angle position of diffracted x-ray, λ = X-ray wavelength.

The distance between atoms varies regularly with the type of materials. Therefore, if the distance between atomic planes is known, one can know the type of constituents of the sample. Also, the peak intensity of diffracted x-rays is proportional to the quantity of a constituent, so that a quantitative analysis can be made by measuring it.

4.5 Internal Stress Measurement

The internal stress in ZnO films was determined by the substrate curvature method. The radius of curvature was measured by a surface profilometer (Tencor P10). The thickness of the deposited films was determined by measuring the step height between masked and unmasked regions on the substrate using the profilometer.

The Tencor P-10 Surface Profiler is a computerized, high-sensitivity surface profiler that measures roughness, waviness, and step height in a variety of applications. It features the ability to measure micro-roughness with 1 Å resolution over short distances as well as waviness over a full, 60-mm scan. The attached computer offers powerful measurement control, data storage, and analysis.

The Tencor P-10 provides the following features:

- Advanced MicroHead II low-force measurement head that precisely measures the surface typography of finely textured samples at sub-angstrom vertical resolution.
- Precise measurement of profiles of roughness less than 1 nm and features below 10 nm, even on ultra-smooth samples.
- Innovative stylus arm, offering an extremely low moment of inertia, reducing sensitivity to environmental noise.
- Advanced digital signal processing (DSP), improving control and accuracy with up to 1 kHz sampling rates for faster scans.
- Constant stylus force control throughout the entire vertical sensor range, by incorporating an intelligent sensor to determine surface topography.

- Extremely low noise characteristics, enabling measurement of step heights with a repeatability of 8 Å maximum in the 6.5 μm range.
- High resolution 3-D imaging of areas more than 500 x 500 μm in size, utilizing the low drift sensor of the head.
- Dual-view optical design (optional), providing a top-down view of an image for stylus positioning, as well as a side-angle view (standard) for checking the stylus tip and measured features.

The Tencor P-10 can profile a variety of materials, including

- Magnetic disks
- Semiconductor wafers
- Precision-machined and polished surfaces
- Ceramics for microelectronics
- Glass for flat panel displays
- Optical surfaces

4.6 Photoluminescence

A photoluminescence (PL) spectrum was acquired in the wavelength range of 350-850 nm at room temperature; the excitation light was the 325 nm line of a He-Cd laser.

The measurement of photoluminescence, because of its intricacy and, many times, very low intensity, is not a simple matter; hence specialized techniques and apparatus are required for this metrology. [53] Luminescence is a phenomenon of the emission by matter of electromagnetic radiation, which, for certain wavelengths or restricted regions of the

spectrum, is in excess of that due to the thermal radiation from the material at the same temperature. This type of radiation depends on the particular host and activator materials, exciting wavelength, and temperature.

By applying the radiometric procedure to the luminescence, the quantities of luminescent radiation and luminescence light are gained. Photoluminescence is a luminescence caused by ultraviolet, visible, or infrared radiation. A special form of photoluminescence is the anti-Stokes luminescence, where an emission at wavelengths shorter than the shortest wavelength of the excited radiation occurs.

The following is a general description of a typical photoluminescence measurement system from the manufacturer Jobin Yvon.

Description

A laser beam is focused on the sample, which is located in the center of the sample compartment. If the energy of photons coming from the laser source is greater than the energy gap of the semiconductor, the sample emits photons. These are collected and analyzed with a dual flat field spectrograph. Two detectors are used, a CCD and an InGaAs array.

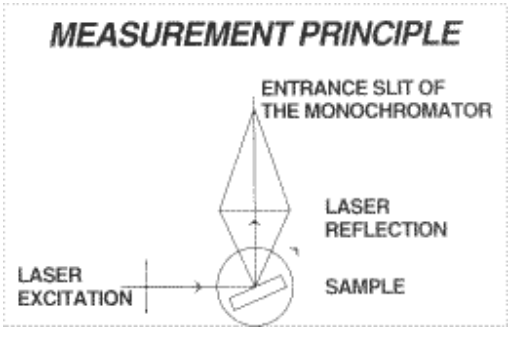

Figure 4.3 Basic principle of photoluminescence measurement

Measurement Procedure

We identify the position of one or several photoluminescence lines, and with the help of mathematical models, determine the composition of the material.

Applications

- Qualitative investigations for semiconductors.
- Fast determination of alloy composition in ternary compounds (GaAlAs, GaInAs, AlInAs...)

System Advantages

The two array detectors, CCD and InGaAs, offer high sensitivity and speed. They can both be mounted simultaneously on a Dual Flat Field Spectrograph allowing full characterization of the sample with ease.

4.7 Optical Transmittance

Transmittance in the range from 190 to 1100nm was measured by ultraviolet-visible (UV-vis) spectrophotometry using HP 8453 spectrophotometer. The transmittance was automatically calibrated against a bare glass as a reference sample, and the absorption coefficient was obtained from the transmittance curve.

The Agilent 8453 spectrophotometer is the core of powerful and productive systems for routine and occasional users that are easy to use and integrate seamlessly into the modern laboratory. The spectrophotometer comes equipped with all the diode-array advantages – fast scanning, excellent sensitivity, virtually absolute wavelength reproducibility, exceptional ruggedness and reliability, minimum maintenance and open sample area, and significant improvements in optical performance. Better than two nanometer resolution, wavelength range of 190 to 1100 nm and less than 0.03 % stray light is standard. Table 4.1 shows the specifications of the UV-Vis spectrophotometer.

Table 4.1: Specifications 8453 UV-Visible Spectrophotometer

Wavelength range	190-1100 nm
Slit width	1 nm
EP resolution test	>1.6 toluene in hexane, ratio abs. at 269 nm/266 nm
Stray light	<0.03 % at 340 nm (NaN02, ASTM) <0.05 % at 220 nm (Nal, ASTM) <1 % at 200 nm (KCI, EP)
Wavelength accuracy	<±0.5 nm - 0.5-second scan (NIST 2034) <±0.2 nm (at 486.0 and 656.1 nm)
Wavelength reproducibility	<±0.02 nm - ten consecutive scans (NIST 2034)
Photometric noise	<0.0002 A - sixty 0.5-second scans at 0 A, 500 nm, rms
Photometric stability	<0.001 A -at 0 A, 340 nm after 1-hour warm up, measured over 1 hour, every 5 seconds, constant ambient temperature.

Chapter 5

Thin Film Characterization

5.1 Structural Properties

5.1.1 Crystal Structure

5.1.1.1 Undoped ZnO Films

ZnO has a wurtzite structure with lattice parameters *a*=0.34982 nm and *c*=0.52066 nm. It consists of interpenetrating oxygen and zinc hexagonal close packed (hcp) lattices. Figure 5.1 shows the XRD patterns of ZnO films deposited on substrates heated from 130°C to 400°C. Only the ZnO (002) peak is observed at 2θ ~ 34.5° for all samples. This indicates that the ZnO films prepared by the FCVA show a good *c*-axis orientation, that is, vertical growth with respect to the substrate. The *c*-axis orientation in ZnO films is due to a self-texturing mechanism as discussed by Jiang *et.al.* [54] They concluded that the film crystal orientation is not affected by the crystallographic structure of a substrate, but is a result of a self-ordering effect caused by the minimization of the crystal surface free energy as well as by the interaction between the deposited material and the substrate surface.

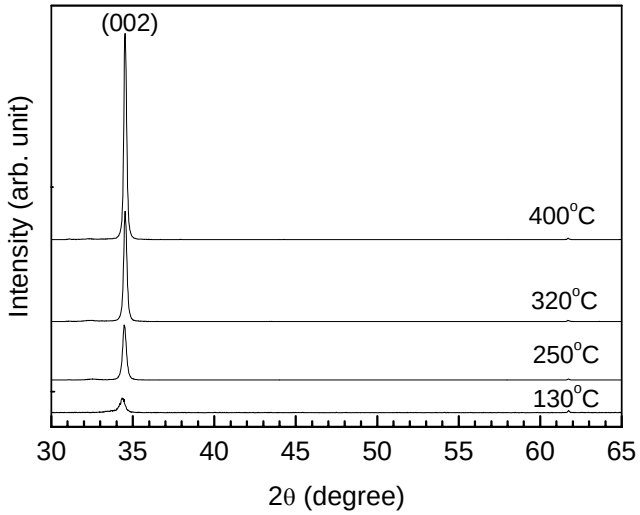

Figure 5.1 X-ray diffraction patterns of the ZnO films deposited under various temperatures.

Figure 5.2 shows a plot of the full width at half maximum (FWHM) of the (002) diffraction peaks as a function of substrate temperature. The FWHM decreases with increase in temperature, indicating an increase in grain size with increasing temperature. The grain size is related to FWHM by the Scherrer formula

$$t = \frac{0.9\lambda}{\Delta\theta \cos\theta_B}, \qquad (1)$$

where t is the grain size, $\Delta\theta$ is the FWHM, λ is the x-ray wavelength, and θ_B is the Bragg angle. The effect of increasing grain size can also be seen from the atomic force microscope (AFM) images from Section 5.1.2. As the film grows thicker, the larger grain is formed via the aggregation of small grains or grain boundary movement.

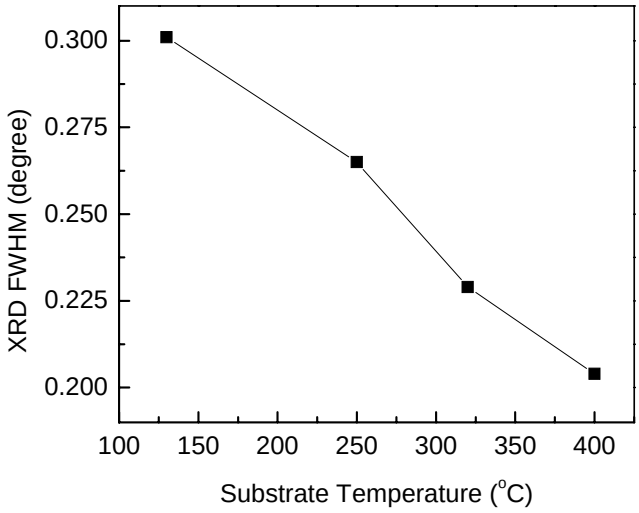

Figure 5.2 The XRD FWHM for samples grown at different temperatures.

Figure 5.3 shows the XRD patterns of ZnO films prepared as substrate bias was varied from -10 to -160V. The curves for the films deposited at bias of -90 and -160V cannot be seen as their intensity peaks, at 100 cps, are too low compared to those for -10 to -40V. This is due to the energetic bombardment on the growing film's surface at high substrate bias like -90 or -160V, which causes defects in the film, hence reducing the crystallinity. The peak positions of XRD patterns for films prepared at bias of -10 to -40V are listed in Table 5.1.

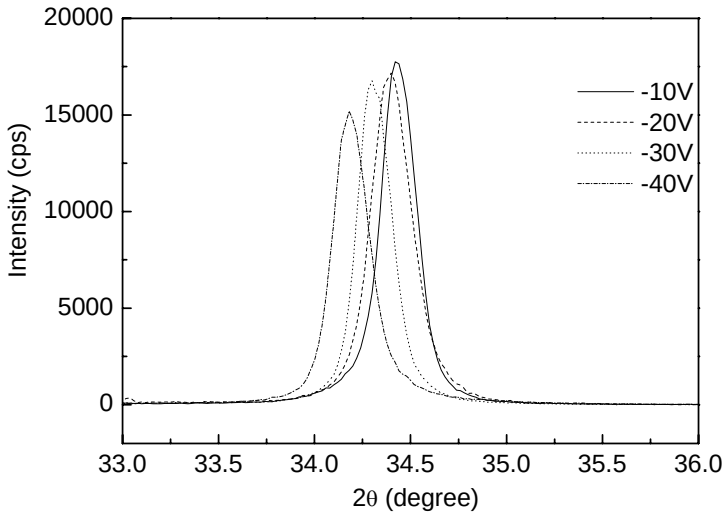

Figure 5.3 X-ray diffraction patterns of the ZnO films deposited at various substrate bias.

Table 5.1: Peak positions of XRD patterns for films prepared at various bias voltages

Substrate Bias (V)	2θ (degree)	Lattice Constant *c* (Å)
-10	34.42	5.207
-20	34.38	5.213
-30	34.29	5.226
-40	34.18	5.243

Based on the XRD data, the lattice parameter of *c* has been estimated in the range of 5.207 to 5.243 Å, which is larger than the American Society for Testing and Materials value of 5.200 Å for bulk ZnO, with the difference caused by stress. The stress parallel to the film surface is given by [55]

$$\sigma_{Film} = \frac{2c_{13}^2 - c_{33}(c_{11}+c_{12})}{2c_{13}} \cdot \frac{c_{film} - c_{bulk}}{c_{bulk}}, \qquad (2)$$

where C_{film} refers to the film lattice constant and C_{bulk} refers to the bulk lattice constant. The elastic constants C_{ij}, of single crystal ZnO have been used: C_{11}=208.8, C_{33}=213.8, C_{12}=119.7, C_{13}=104.2 GPa. This yields the following numerical relation for the stress derived from XRD:

$$\sigma_{Film} = -233 \times \frac{c_{film} - c_{bulk}}{c_{bulk}}. \quad (3)$$

Since the value of c for all our films are larger than that for bulk ZnO, the resulting stress is compressive. This is in agreement with the observation made in Section 5.1.2. Figure 5.4 shows the stress calculated from XRD results for films deposited at various substrate bias.

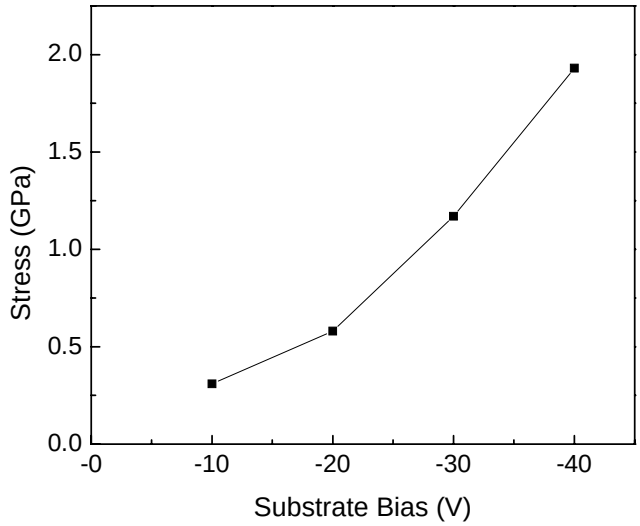

Figure 5.4 Stress derived from XRD patterns for samples prepared at different substrate bias.

5.1.1.2 ZnO:Al Films

Figure 5.5 shows the XRD patterns of ZnO:Al films deposited on substrates with temperatures of 100 and 350°C, with O_2 pressure kept at 5×10^{-4} Torr. The typical thickness of our films is 250nm. Only the ZnO (002) peak is observed at $2\theta \sim 34.5°$ for all the samples. This indicates that the ZnO:Al films prepared by the FCVA show a good *c*-axis orientation, that is, vertical growth with respect to the substrate. The *c*-axis orientation in ZnO:Al films is due to a self-texturing mechanism as discussed by Jiang *et.al.* [54]

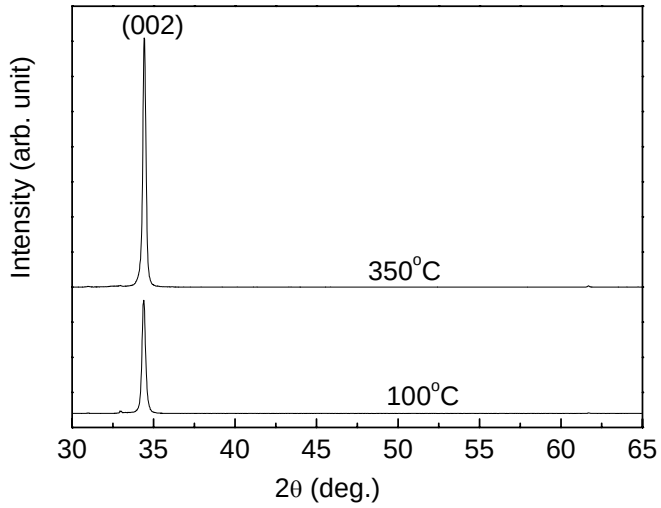

Figure 5.5 X-ray diffraction patterns of the ZnO:Al films deposited under various temperatures.

Cross-sectional SEM micrograph of ZnO:Al film prepared at temperature of 250°C and pressure of 5×10^{-4} Torr is depicted in Figure 5.6. The film shows a high degree of alignment of the columnar structure, thus confirming the *c*-axis orientation growth as indicated by XRD pattern of the films. Polley *et.al.* [56] reported on a zone model for ZnO deposited by combustion chemical vapor deposition. In their case, the ZnO films deposited at low temperatures (177°C and 289°C) were amorphous with deep voids between nodular growths. There is no amorphous phase in the films prepared by the FCVA, even the films prepared at room temperature are polycrystalline and exhibit columnar structure, without the presence of voids. This is largely due to the energetic species in FCVA, giving rise to the activation of surface diffusion, which promotes the formation of dense polycrystalline films. The characteristic columnar morphology can be attributed to the zone *II* according to the structure zone model (SZM) of Thornton. [57] In the films prepared by the FCVA, the morphology corresponding to the zone *T* in Thornton's model was not observed, which is similar to the observation by Mirica *et.al.*[58]

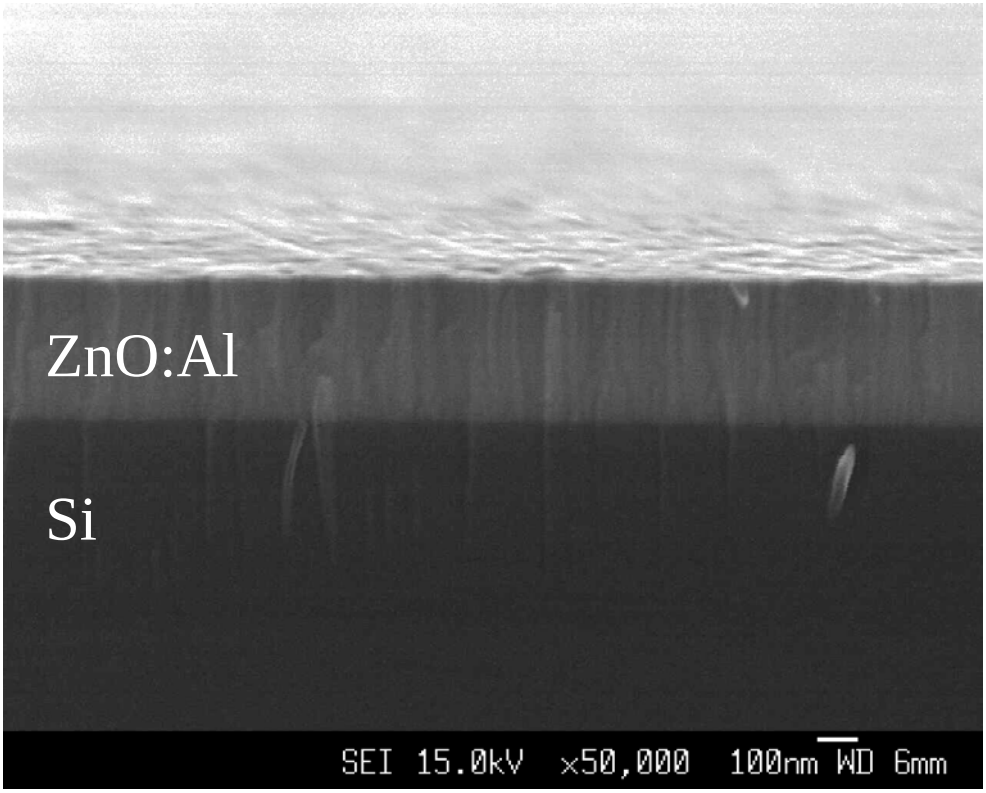

Figure 5.6 SEM micrograph of cross section of the ZnO:Al film on Si substrate deposited at temperature of 250 ℃ and pressure of 5×10^{-4} Torr.

5.1.2 Internal Stress and Surface Morphology

The typical thickness of the ZnO films used in the present study is 250nm with a deviation of 10%. The internal stress was determined by the radius of curvature technique which compares the curvatures of the bare silicon substrates and substrates coated with a film. The stress is given by Stoney's equation

$$\sigma = \frac{E_s}{6(1-\upsilon_s)} \frac{t_s^{\,2}}{t_c} \left(\frac{1}{R} - \frac{1}{R_0} \right), \qquad (4)$$

where E_s, ν_s, t_s, and t_c are the Young's modulus, Poisson's ratio, thickness of the substrate, and thickness of the films, respectively. R and R_0 are the radii of curvature of the film substrate composite and bare substrate, respectively. [59] For each film examined by the surface profilometer, the radius of curvature at different locations was measured and averaged, with a standard deviation of 5%. The substrates were measured prior to deposition to yield R_0.

Stress in zinc oxide films contains a thermal component and an intrinsic component. Figure 5.7 shows the dependence of the internal stress in ZnO films on the deposition temperature. The thermal stresses are a result of differences in the thermal expansion coefficient of the coating and the substrate, and are given by Bull [60]

$$\sigma = \frac{E}{1-\nu} \Delta\alpha \, \Delta T \,, \qquad (5)$$

where E and ν are Young's modulus and Poisson's ratio of the films, respectively, Δα is the difference in expansion coefficients of the substrate and film, and ΔT is the difference between the coating temperature and room temperature. The thermal expansion coefficient of zinc oxide is larger than that of silicon, resulting in a tensile lateral stress in

the zinc oxide film due to cooling after deposition. The α of bulk ZnO (4.75×10^{-6}/K) is used here, as obtained from the product specification data of Yamanaka Semiconductor Co., Ltd. The α of Si used is 2.59×10^{-6}/K. [61]

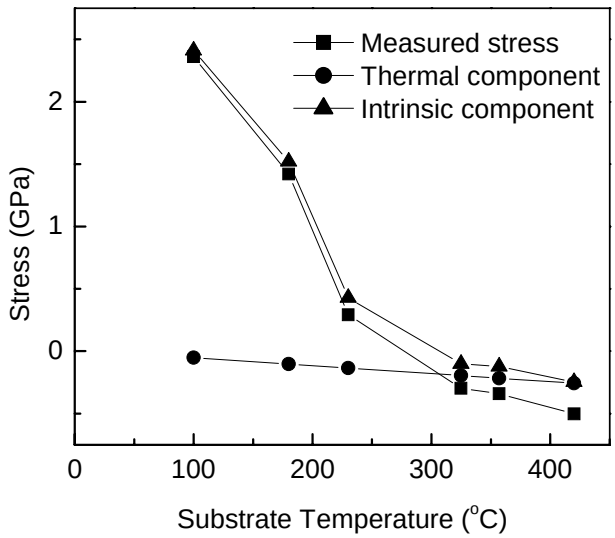

Figure 5.7 Dependence of the internal stress in the ZnO films on the deposition temperature.

The intrinsic stress in ZnO film is predominantly compressive. Intrinsic compressive stresses exist almost in all covalent solid films deposited by physical vapor deposition associating with the bombardment of energetic species during deposition. The intrinsic compressive stresses in the films have been proposed to be originated from the "atomic peening" mechanism. [62] For the films deposited at the low temperature, the energetic ions can be sub-implanted into the subsurface, and the surface atoms can also be knocked deeper into the subsurface of the growing films by the bombardment of energetic ions or atoms. Due to the low mobility of the atoms in the films, these sub-implanted or knocked

atoms can be trapped in the subsurface. The associated additional volume in the constrained layer leads to an expansion of the film outwards from the substrate, but the film is not free to expand and the entrapped atoms cause serious strain, and, therefore, the high intrinsic stress in the films. In addition, due to the non-equilibrium process, these sub-implanted or knocked atoms can be trapped in the non-equilibrium position. The existence of Zn or O atoms in the non-equilibrium position causes additional strain in the films, which will also contribute to the high stress in the films.

As the deposition temperature is increased, the mobility of atoms in the films increases greatly. The atoms can easily diffuse from one to another position. Then, the atoms trapped in the non-equilibrium position due to the sub-implantation or knock-on processes can adjust the position and shift outside to a more equilibrium position, which can release the strain in the films, and, therefore, the decrease of the compressive stress.

Furthermore, there exists a tensile component of the intrinsic stress which becomes observable at high temperature. This tensile stress is caused by grain boundary relaxation.[63, 64, 65]

Residual tensile stresses are believed to result from grain growth when structural relaxation lags the deposition rate. Structural relaxation occurs in order to minimize the free energy of the system and results in a reduction of the specific volume of the film as long as the film is unconstrained. However, if the film is geometrically constrained by the substrate, volumetric relaxation is inhibited and a residual stress is produced in the film and substrate. The resultant intrinsic stress curve goes from compressive to weakly tensile as the substrate temperature increases, being the result of the combination of a

compressive component due to atomic peening and a tensile component due to grain boundary relaxation.

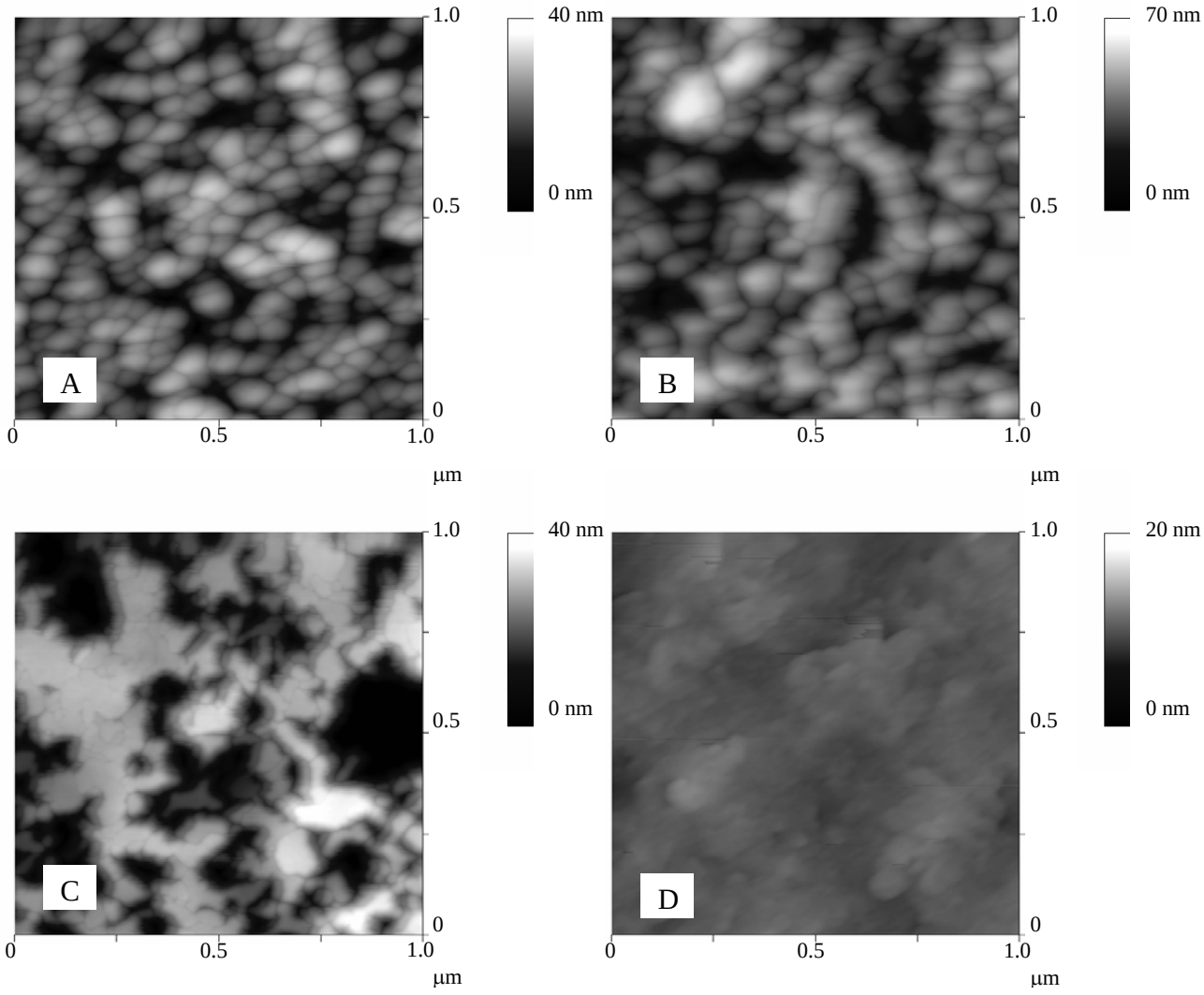

Figure 5.8 AFM images of ZnO films deposited at temperatures of: (A) 180℃, (B) 320℃, (C) 360℃, and (D) 420℃.

Figure 5.8 shows the AFM image of the ZnO films deposited at temperatures of: (A) 180°C, (B) 320°C, (C) 360°C, and (D) 420°C, respectively. The thickness of the films is

almost constant for different temperatures, varying between 235 and 265nm. The surface morphology varies significantly with deposition temperature. The root mean square (RMS) surface roughness increased with an increase in temperature till it reached a maximum of 9.75nm at 360°C, beyond which surface roughness decreased. Grain size increased as the deposition temperature was raised, and this initially contributed to an increase in roughness. As temperature was further raised, the surface roughness decreased because of thermally activated diffusion which promotes two dimensional growth. The above postulation may be supported by the x-ray diffraction experiments, which were performed in the Bragg-Brentano configuration. The occurrence of two-dimensional growth is indicated by the increase in crystallinity with temperature, which can be observed from the diffraction peaks in Figure 5.1 (from Section 5.1.1). Only the ZnO (002) peak is observed for all the samples, indicating that the ZnO films prepared by filtered cathodic vacuum arc are *c*-axis oriented.

Figure 5.9 shows the internal stress in ZnO films as a function of the substrate bias. The internal stress, which is compressive in all the deposited films, is strongly dependent on the substrate bias. As the substrate bias is increased from -10V, the internal stress increases rapidly from 0.2 GPa, reaching the maximum of 3.1 GPa at a bias of –65V, then decreases gradually. The rate of the decrease in stress is very low at substrate bias more negative than –100V, indicating a limit to the stress relaxation through an increase of bias, and the compressive stress appears to converge to a value of about 1.5 GPa.

When investigating the relationship between substrate bias and internal stress, the influence of thermal stress on the variation of the internal stress can be ignored, because all the films were deposited at the same deposition temperature.

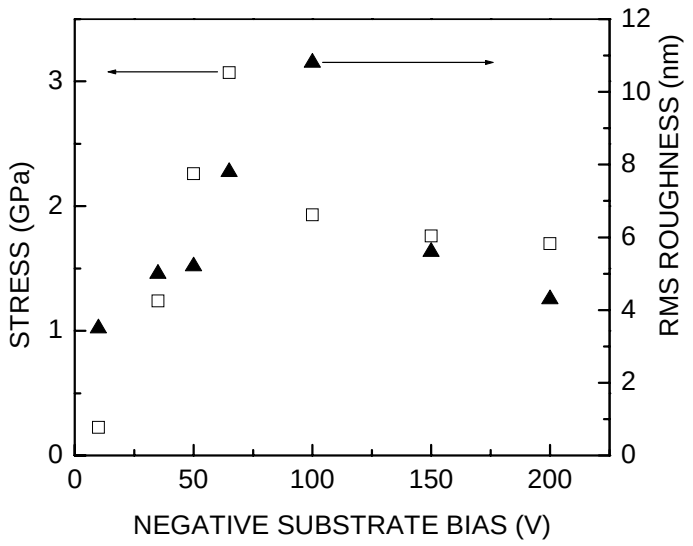

Figure 5.9 Dependence of the internal stress and rms roughness in the ZnO films on various substrate bias.

As mentioned above, the intrinsic compressive stresses in the films deposited under ionic bombardment originate from the atomic peening mechanism. However, at higher bias voltages, the high ion deposition energy causes stress relaxation due to "thermal spike".[66] A significant fraction of the energy of a bombarding ion is transferred to violent motion of the atoms in the area of the impact. This intense local heating, or "thermal spike", can provide the energy required to release implanted atoms from their metastable positions within the film, hence bringing forth stress relaxation.

The total intrinsic stress in the films is a result of the competition between stress generation and stress relaxation. For the films deposited at a substrate bias of –10V, the low ion energy leads to the formation of films that exhibit low internal stress. The increase of substrate bias results in the linear increase of ion energy, resulting in an

increase of the atomic peening effect, which leads to the rapid increase of internal stress. However, at the bias of above –65V, more energy can be transferred to the film atoms by the bombardment of the energetic ions. The effect of stress relaxation due to thermal spike begins to play an important role, leading to the decrease of internal stress.

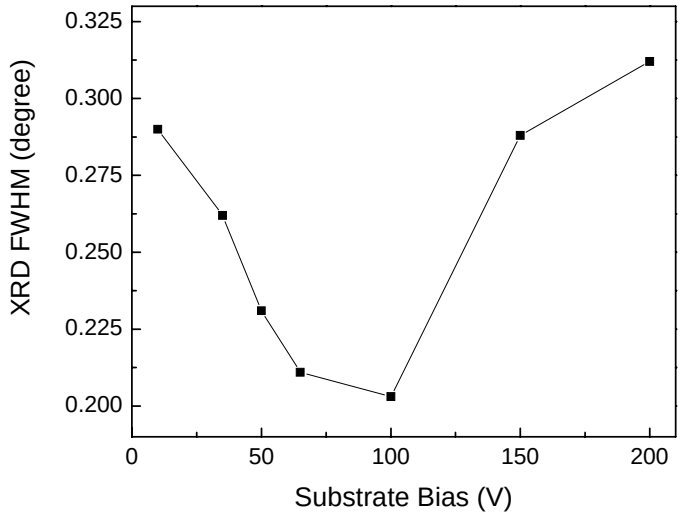

Figure 5.10 The XRD FWHM for samples grown at different substrate bias.

The surface morphology varies significantly with substrate bias. Figure 5.9 (previous page) shows the RMS surface roughness in ZnO films as a function of the substrate bias. The kinetic energy of the ions impinging on the substrate increased with increasing substrate bias, and this initially assisted the growth of larger crystalline grains, resulting in greater roughness. This is in agreement with the XRD measurements (Figure 5.10), with narrower FWHM indicating the presence of larger crystalline grains. Further increase in kinetic energy of the ions gives rise to smaller crystallites, hence a lower value for surface roughness, as intense bombardment of the film surface inhibits the growth of large crystallites.

For the films deposited at the same temperature, 260°C, the resulting stresses vary significantly with the variation of oxygen pressure from 3.8×10^{-5} to 3.4×10^{-4} Torr (Figure 5.11). The compressive stresses decreased with an increase of the pressure. This is similar to ZnO thin films grown by Hinze *et al.* [59], with working pressure from 9.8×10^{-4} to 2.2×10^{-2} Torr.

At low pressures, energetic particles coming from the target as positive ions can strike the film surface with substantial kinetic energy, giving rise to compressive stresses. The mechanisms developed by Windischmann [67, 68] can be invoked to explain the origin of compressive intrinsic stresses in these dense films.

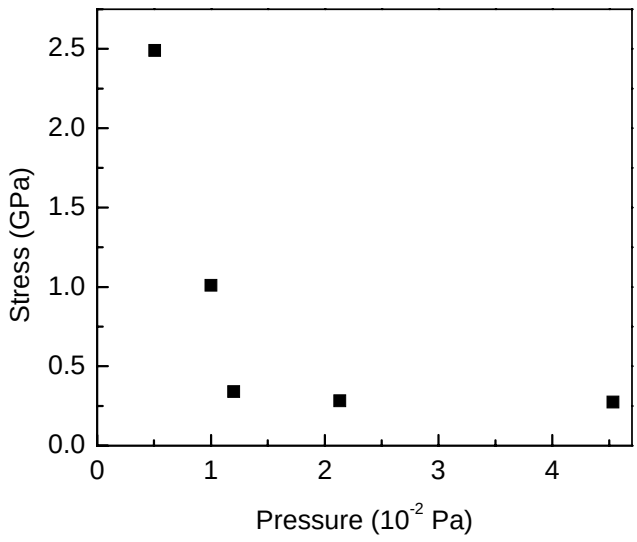

Figure 5.11 Dependence of the internal stress in the ZnO films on the gas pressure.

The forward sputtering model proposed by Windischmann corresponds to a quantitative development of the peening mechanism discussed by Hoffman [62] who suggested that the compressive stress in sputter-deposited films was caused by the bombardment of the film

surface by energetic species. As the pressure in the deposition chamber is increased, particle scattering phenomena caused by collisions with residual gas atoms or molecules contribute to reduce the kinetic energy of species arriving at the film surface. As a result, the effect of atomic peening is weakened, leading to a reduction in compressive stress.

5.2 Electrical Properties

5.2.1 Undoped ZnO Films

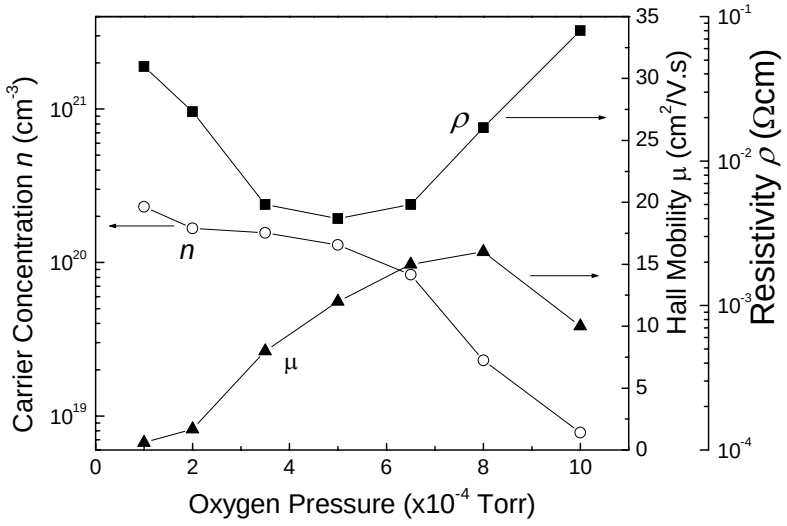

Figure 5.12 Plot of resistivity, carrier concentration and Hall mobility as functions of oxygen pressure.

Figure 5.12 shows the plot of resistivity, carrier concentration and Hall mobility as functions of oxygen pressure. The films were deposited under room temperature. All the films are in *n*-type conduction; their resistivities first decrease with an increase of the oxygen pressure and reach a minimum resistivity of 4.1×10^{-3} Ωcm at pressure of about 5×10^{-4} Torr and then increase. The electrons in undoped ZnO films are normally attributed to intrinsic donors, but oxygen vacancies and zinc interstitials have frequently been invoked as the source of electrons.[69] From Figure 5.12, we see the carrier concentration decreases with an increase of the oxygen pressure. The oxygen vacancy

was originally considered responsible for the observed *n*-type conduction in ZnO.[70] Recently more experimental and theoretical work has found that the zinc interstitial is the main cause of electrons in undoped ZnO. Electron irradiation experiments by Look *et. al*. showed that the zinc interstitial is most likely the cause of a shallow donor in ZnO. [71, 72] Theoretical calculations indicate that the zinc interstitial is a shallow donor, and that the oxygen vacancy is a deep donor about 0.6 or 0.7 eV from the conduction band. [73] Hydrogen acts as a shallow donor and is suggested to be responsible for *n*-type conduction in nominally undoped ZnO films. [74, 75, 76] However, in our case, the hydrogen concentration in the film should be very trivial if it even exists. If the background hydrogen partial pressure in the reactive chamber is large enough and it acts as a determining factor in the electrical properties of the films, we would not expect the carrier concentrations of the films to display such regular strong oxygen pressure dependence behavior. For the same reason, the effects of other impurities, such as aluminum, can also be excluded, so the zinc interstitial should be the most likely to explain the observed high carrier concentrations. Hall mobility reflects the scattering processes of carriers in the films. In an undoped polycrystalline film, carriers are scattered mainly by intrinsic defects and grain boundaries, and other mechanisms such as lattice vibration scattering can be neglected. The grain boundary scattering depends on the grain size and electron mean free path in the films. The mean free path of electrons in the films can be roughly estimated by the highly degenerate electron model using the formula, [77]

$$l = \left(\frac{h}{2e}\right)\left(\frac{3n}{\pi}\right)^{1/3}\mu, \qquad (6)$$

where n is the carrier concentration and μ is the Hall mobility. Using the data in Figure 5.12, the mean free path of the electron is estimated to be below 2 nm. The grain sizes are about tens of nanometers as characterized by AFM, so intragrain scattering is dominant. The defects within the grains cause the observed low Hall mobility. The Hall mobility increases gradually with the pressure up to 8×10^{-4} Torr, and it decreases slightly with a further increase in pressure. The mobility values are lower than those of the films deposited at high temperature, but are similar to the films deposited at room temperature by other methods. [19, 78] The ZnO films are stable in air after storage for several months. Their conductivities remain unchanged. Annealing experiments indicate that the films can withstand temperatures up to 200°C in air without changing their electrical and optical properties.

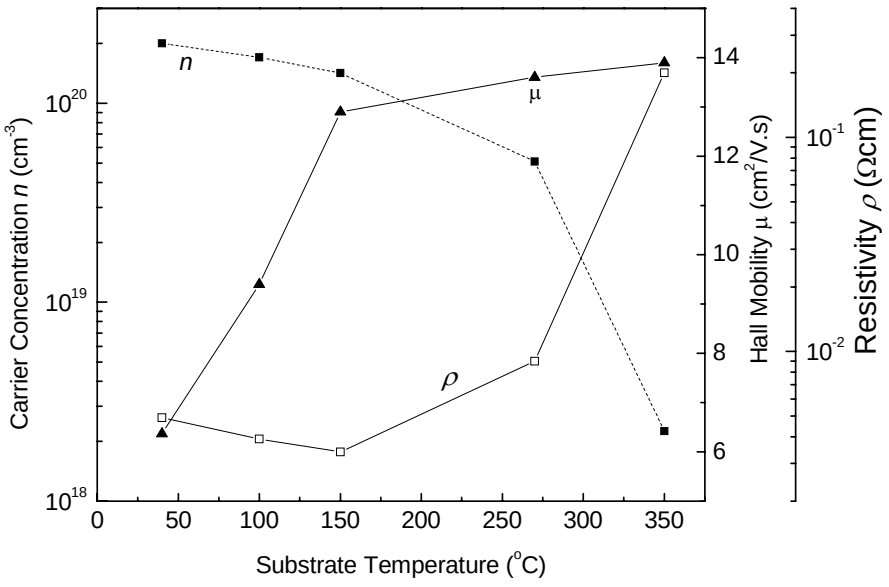

Figure 5.13 Resistivity, carrier concentration and Hall mobility as functions of substrate temperature for undoped ZnO films.

Figure 5.13 shows the plot of resistivity, carrier concentration and Hall mobility as functions of substrate temperature for undoped ZnO films. The oxygen pressure for all the films was 7 x 10^{-4} Torr. The resistivity initially decreases as the temperature is increased up to 150°C, after which the resistivity increases rapidly with temperature. The lowest resistivity is 3.4 x 10^{-3} Ωcm, which is obtained for the substrate temperature of 150°C.

The mobility increased as substrate temperature is increased, and this causes a reduction in resistivity for films prepared at substrate temperatures below 150°C. Crystallite size increases as the substrate temperature is increased, and this leads to reductions in grain boundary scattering due to charge carriers, which consequently increases the mobility for the obtained films. At temperatures above 150°C, the resistivity increases in spite of the increase in mobility as the reduction in carrier concentration is far greater than the gain in mobility.

In the ZnO films, n-type carriers are generated by interstitial Zn atoms acting as donors, thus, a fall in the concentration of interstitial Zn will lead to a fall in carrier concentration. Igasaki *et.al.* [79] reported that the carrier concentration decreases continuously with increasing temperature to 300°C for ZnO:Al films having thickness in the range from 160 to 250 nm, and they attribute this to the reduction in the number of native donors because of the high vapor pressure of zinc, which results in evaporation of Zn at higher substrate temperature. This is similar to our observation for undoped ZnO films.

5.2.2 ZnO:Al Films

A widely reported method to achieve low resistivity is to dope ZnO with aluminum. The electrical properties of samples prepared by several Al-doped Zn targets were investigated. Figure 5.14(a) shows the plot of resistivity, carrier concentration and Hall mobility as a function of substrate temperature for ZnO:Al films prepared with a Zn-Al alloy target with 5 at.% of Al. The resistivity initially decreases as the temperature is increased up to 150°C, after which the resistivity increases rapidly with temperature. The lowest resistivity for the films was $8x10^{-4}$ Ωcm at a substrate temperature of 150°C. The explanation for this trend in the resistivity is the same as that provided (in the previous page) in the case of undoped ZnO films.

Figure 5.14(b) shows the plot of resistivity, carrier concentration and Hall mobility for samples prepared with Zn-Al targets of various Al contents. The films were deposited at room temperature. The carrier concentration increased with increasing Al content, leading to reduction in the resistivity. Although the mobility decreased slightly with increasing Al content, the decrease was not sufficient to affect the trend of reduction in resistivity with increasing Al content.

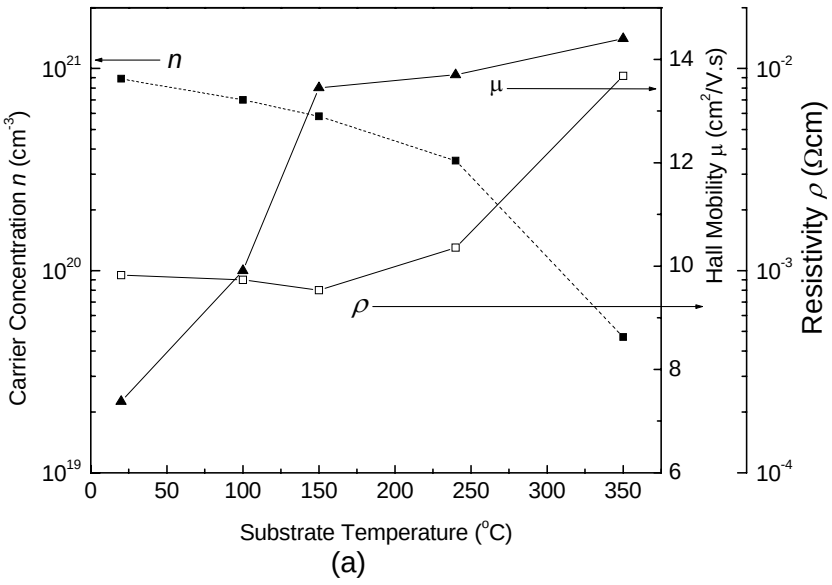

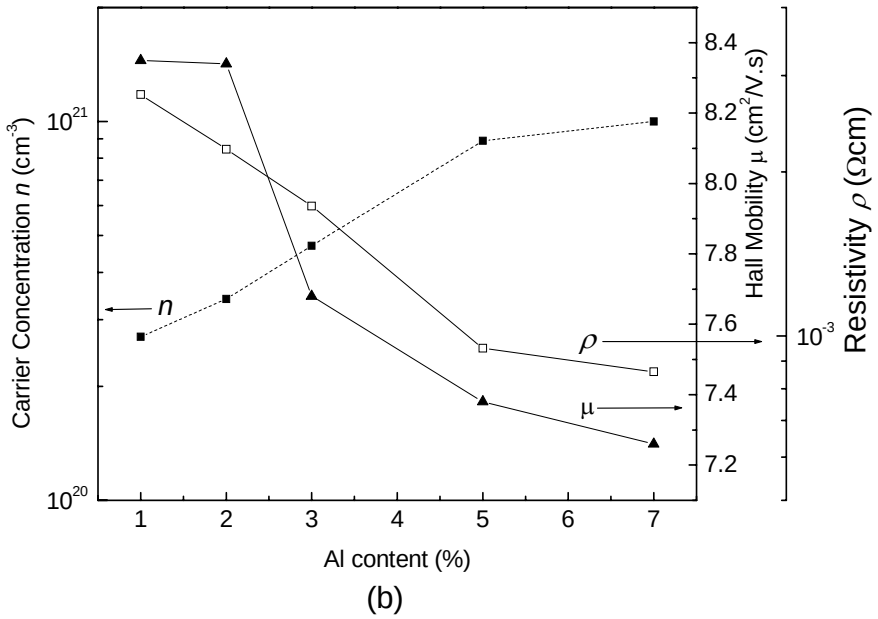

Figure 5.14 Resistivity, carrier concentration and Hall Mobility as a function of (a) substrate temperature for ZnO:Al (5 at.%), and (b) Al content of films deposited at room temperature. The films were deposited at an O_2 pressure of $5x10^{-4}$ Torr.

5.3 Optical Properties

5.3.1 Undoped ZnO films

Figure 5.15 shows the optical transmittance of ~200nm thick ZnO films deposited at different pressures of 2×10^{-4}, 4×10^{-4}, 5×10^{-4}, 6×10^{-4}, and 1×10^{-3} Torr. The films were deposited at room temperature. The average optical transmittance of the films, except that deposited at 2×10^{-4} Torr, in the visible spectrum is about 90%. It is seen that the transmittance of the films improves with an increase of the oxygen pressure. A steep falloff is observed at around 380nm in the films deposited at oxygen pressure above 2×10^{-4} Torr, which is characteristic of high crystal quality ZnO films. The oscillations in the spectra are caused by optical interference on the smooth surface. The spectrum of the film deposited at 2×10^{-4} Torr is similar to those of amorphous material and no sharp absorption edge appears in it. This shows that the crystal quality deteriorates for strong oxygen deficiency conditions at low gas pressure. As the pressure is increased, the absorption edge shifts to the longer wavelength region. The shift of the absorption edge to the longer wavelength region is caused by decreased Burstein-Moss shift. [80, 81] The decrease in Burstein-Moss shift is due to the decrease of carrier concentration (n_e) with increase in oxygen pressure.

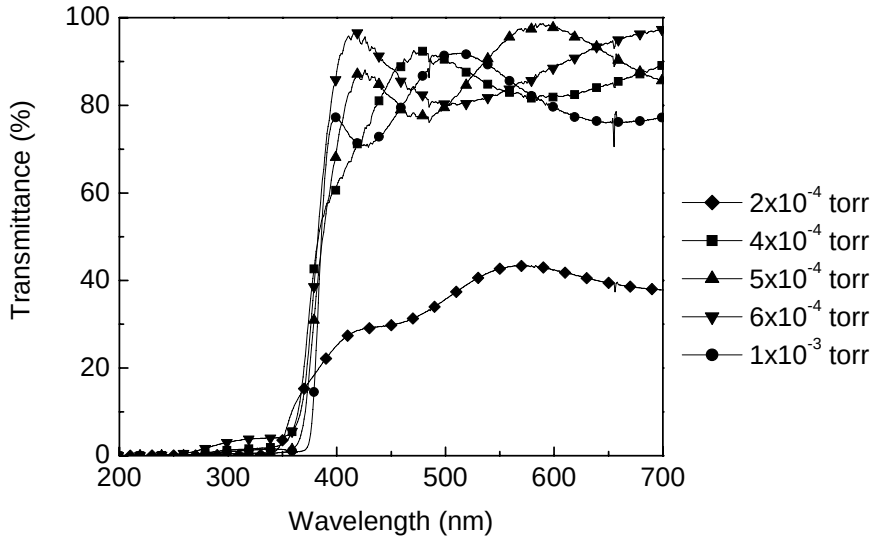

Figure 5.15 Optical transmittance of ZnO films prepared at different oxygen pressures.

The optical absorption coefficient, α, is defined as

$$I = I_O e^{-\alpha t} \tag{7}$$

where I is the intensity of transmitted light, I_O is the intensity of incident light, and t is the thickness of the ZnO film (here, 200nm). Figure 5.16 shows the variation of α^2 with respect to photon energy. In the direct transition semiconductor, the optical absorption coefficient (α) and the optical energy band gap (E_g) are related by,

$$\alpha \propto \left(h\nu - E_g\right)^{1/2}, \tag{8}$$

where h is Planck's constant, and ν is the frequency of the incident photon. The linear dependence of α^2 on $h\nu$ indicates that ZnO films are direct transition type semiconductors. The photon energy at the point where the linear fit of α^2 crosses zero

equals E_g. Then E_g is determined by the extrapolation method.

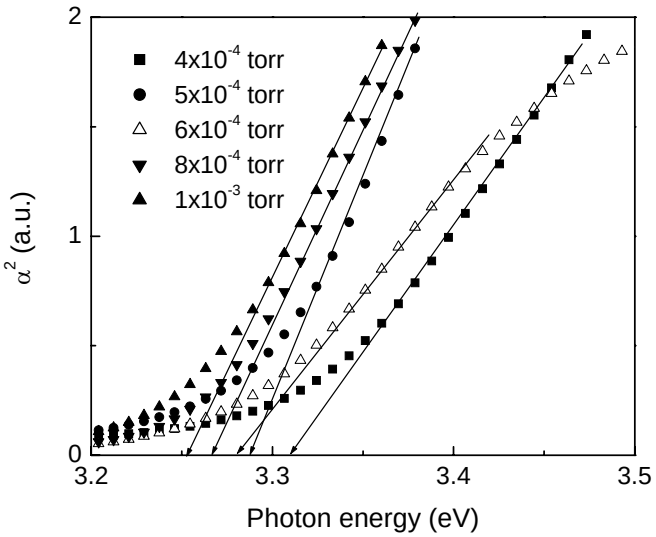

Figure 5.16 Square of the absorption coefficient as a function of photon energy for ZnO films deposited under various oxygen pressures.

Table 5.2: Optical band gap for films prepared at various oxygen pressures

Oxygen Pressure (torr)	Optical Band Gap (eV)
$4x10^{-4}$	3.31
$5x10^{-4}$	3.29
$6x10^{-4}$	3.28
$8x10^{-4}$	3.27
$1x10^{-3}$	3.25

The optical band gap for the films deposited at different pressures is listed in Table 5.2 above.

Burstein [82] pointed out that the increase of the Fermi level in the conduction band of the degenerate semiconductor leads to the energy band widening (blue shift) effect. The energy band gap widening (ΔE_g) is related to n_e through the following equation,

$$\Delta E_g = \frac{h^2}{8m^*}\left(\frac{3}{\pi}\right)^{2/3} n_e^{2/3}, \qquad (9)$$

where h is Planck's constant and m^* is the electron effective mass in conduction band.

The mechanism behind the Burstein-Moss shift is known as a "band-filling" or "state-filling" mechanism, because the change in absorption results from the filling of states with electrons that then prevent further absorption into those states by the Pauli's Exclusion Principle.

The carrier concentration decreased with an increase in pressure, there is thus a red shift effect (that is, shift toward narrower band gap with increase in pressure). An increase in pressure has the effect of reducing the concentration of interstitial zinc atoms in the ZnO films, contributing to a reduction in carrier concentration.

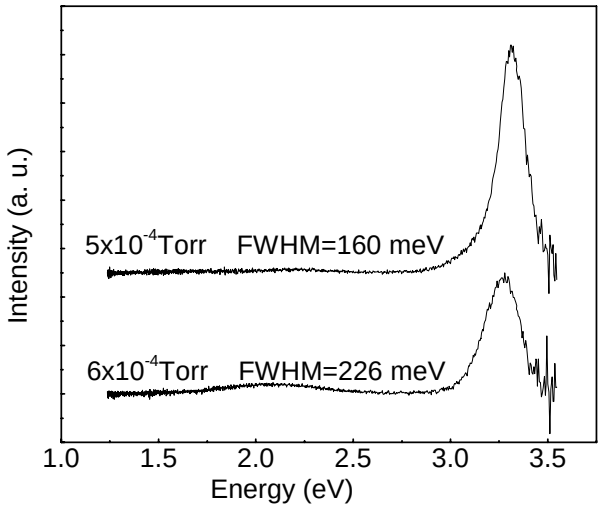

Figure 5.17 Room-temperature PL spectra of ZnO films deposited at different pressure. The films were prepared under room temperature.

Figure 5.17 shows the room-temperature photoluminescence (PL) spectra of ZnO films deposited at different pressures. The FWHMs of the PL spectra of the films prepared at $5x10^{-4}$ Torr and $6x10^{-4}$ Torr are 160 meV and 226 meV, respectively. For the film deposited at $6x10^{-4}$ Torr, an emission at around 2.2 eV (yellow emission) is observed. This emission has been attributed by various authors to the recombination of free electrons with holes via oxygen vacancies. [83] Vanheusden *et al.* [84] found that the intensity of the deep level emission in ZnO powder correlates very well with both the free-carrier electron density n_e and the paramagnetic oxygen-vacancy density, thus suggesting the yellow emission is due to oxygen vacancy. Plasma hydrogenation has been found to passivate the deep level emission and enhance the band-edge recombination, because oxygen vacancies can be terminated by the excited hydrogen. Although hydrogen has not been introduced in our deposition process, no deep level emission can be observed for the

film prepared at $5x10^{-4}$ Torr. It is believed that the high density films prepared by the FCVA has very low concentration of oxygen vacancies, it thus has the same effect as hydrogenation.

5.3.2 ZnO:Al films

ZnO:Al thin films were prepared at substrate temperature that ranged from 90 to 350°C, with the pressure kept at $5x10^{-4}$ Torr. Figure 5.18 shows the optical transmittance and the relation between α^2 and $h\nu$ for the films prepared at different substrate temperatures. For all the films, a high transmittance of about 90% was obtained in the visible wavelength range. As the temperature is increased, the absorption edge shifts to the longer wavelength region, this is attributed to reduction in the Burstein-Moss shift. The optical band gap is then estimated by the extrapolation method as described previously. The optical band gap for the films deposited at the temperatures of 90, 140, 230, 300, and 350°C, are 3.31, 3.30, 3.28, 3.27, and 3.26eV respectively.

As substrate temperature is increased, the concentration of interstitial Zn atoms in the ZnO:Al film is reduced, leading to a reduction in carrier concentration. This reduction in carrier concentration brings about a reduction in the Burstein-Moss shift. The optical band gap becomes narrower as a result.

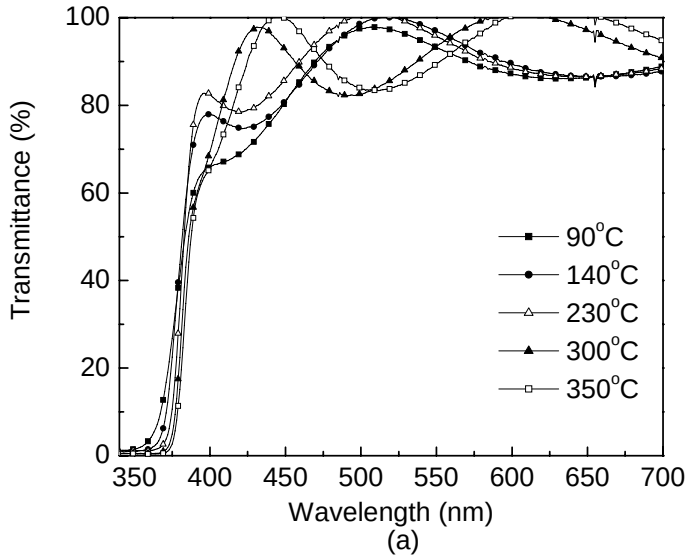

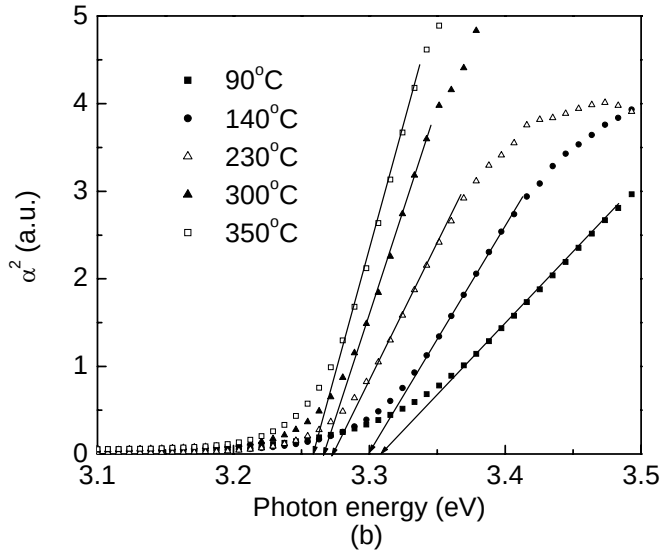

Figure 5.18 (a) Optical transmittance spectrum and (b) square of the absorption coefficient as a function of photon energy for ZnO:Al films prepared at different substrate temperatures.

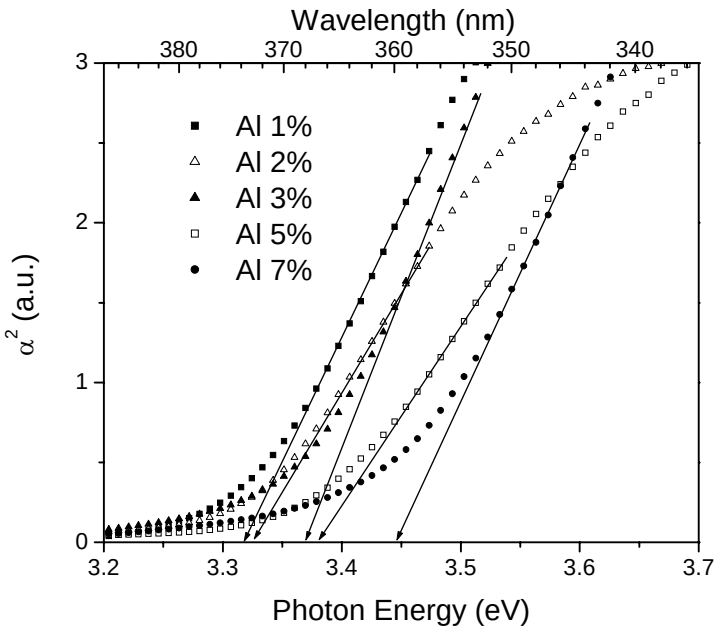

Figure 5.19 Square of the absorption coefficient as a function of photon energy for ZnO films prepared with Al-doped Zn targets which had aluminum contents of 1, 2, 3, 5 and 7%, respectively.

Figure 5.19 shows the plot of α^2 versus $h\nu$ for ZnO:Al films prepared using Al-doped Zn targets with various Al contents. The films were deposited at room temperature with a pressure of $5x10^{-4}$ Torr. Doping ZnO films with Al increases the carrier concentration, and due to the Burstein-Moss effect, the absorption edge shifts to higher energy region.

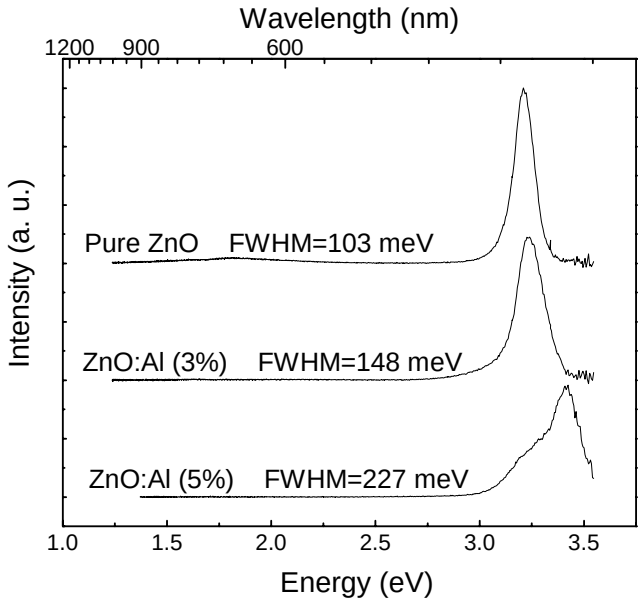

Figure 5.20 Room-temperature PL spectra of pure ZnO, ZnO:Al (3 at.%) and ZnO:Al (5 at.%).

Figure 5.20 shows the room-temperature PL spectra of undoped ZnO and ZnO:Al films. The PL peak shifts to region of higher photon energy with increasing Al concentration, indicating a broadening of band gap, which is in agreement with the observation from the optical absorption measurements. For all three films, no deep level emission can be observed. It is possible that defect states are created when ZnO is doped with Al, allowing for the electron-hole recombination through the defect states. As a result, PL bands were broadened with increasing Al content. Further work needs to be done to verify the reason behind this broadening of the peak.

Optical Characterization in near-Infrared Spectrum

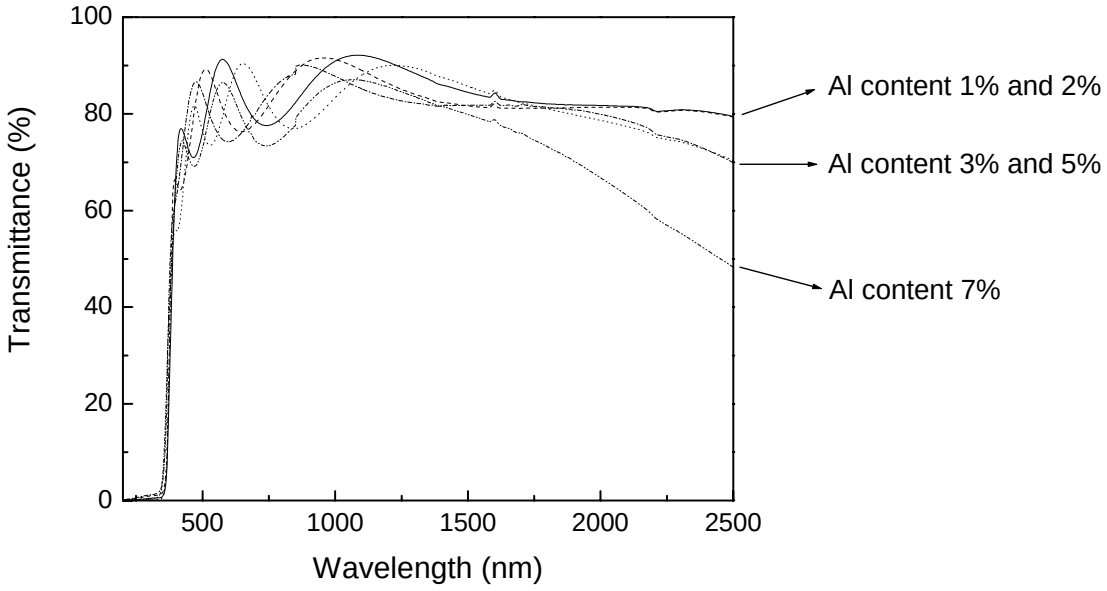

Figure 5.21 Variation of transmittance with various Al contents in the ZnO:Al films.

ZnO film reflects in the infrared region, and this reflection is greater when the film is doped with Al. Similar to the approach by Z. L. Pei *et al.*, [85] it is assumed here that T ≈ 1-R, where T is transmittance and R is reflectance. It can be seen from Figure 5.21 that films with higher Al content had higher IR reflectance. In other words, films with lower resistivity exhibit higher reflectance and a higher IR edge shift to near IR, since higher Al content gives lower resistivity. It can further be deduced that samples with lower sheet resistance had higher infrared reflectance.

For highly degenerately doped semiconducting films, they behaved as metalloid due to the more than 10^{20} cm^{-3} carrier concentration. Thus, the infrared reflectance could be

discussed based on Drude theory. G. Frank [86] suggested that the infrared reflectance for low-resistivity films could be expressed as

$$R = 1 - \frac{4\pi\varepsilon_0 c_0}{en\mu d} \tag{10}$$

$$R_{\square} = \frac{1}{\sigma d} = \frac{1}{en\mu d} \tag{11}$$

$$R = 1 - 4\pi\varepsilon_0 c_0 R_{\square} \tag{12}$$

where ε_0 is the free space dielectric constant, n is the carrier concentration, d is the thickness of film, μ is the carrier mobility, and $R_{\square}$ is the sheet resistance.

Equation (12) reveals that the infrared reflectance would increase with the decrease of sheet resistance as well as the increase of the thickness of the film. At present, due to their high infrared reflectance property, ZnO:Al films have many potential applications, such as electrochromic coating on architectural glazing, heat mirror, incandescent bulbs, reflector-absorber tandem for photothermal conversion, etc.

5.4 Films on Polymer Substrates

Figure 5.23 ZnO deposited on plastic and glass substrates

Figure 5.23 shows a picture of ZnO grown on plastic substrates. ZnO films with low resistivity (~$3x10^{-3}$ Ωcm), high transparency (~90%) were deposited on polyethylene naphthalate (PEN) substrates. The films were prepared at room temperature and the pressure was varied from $3x10^{-4}$ to $1x10^{-3}$ Torr. Figure 5.24 shows the transmittance plot of the films.

The resistivity of ZnO:Al films deposited on polymer substrates was found to be even lower than that obtained in section 5.2.2, due to the fact that the samples were grown at a later stage in the research effort, and is a result of further optimization of the deposition system. Figure 5.25 shows the relation between resistivity and oxygen pressure (with substrate temperature held constant at 80°C), giving a minimum resistivity of 1×10^{-4} Ωcm. As expected, the resistivity increased with increase in oxygen pressure, caused by a reduction in interstitial zinc and, hence, carrier concentration.

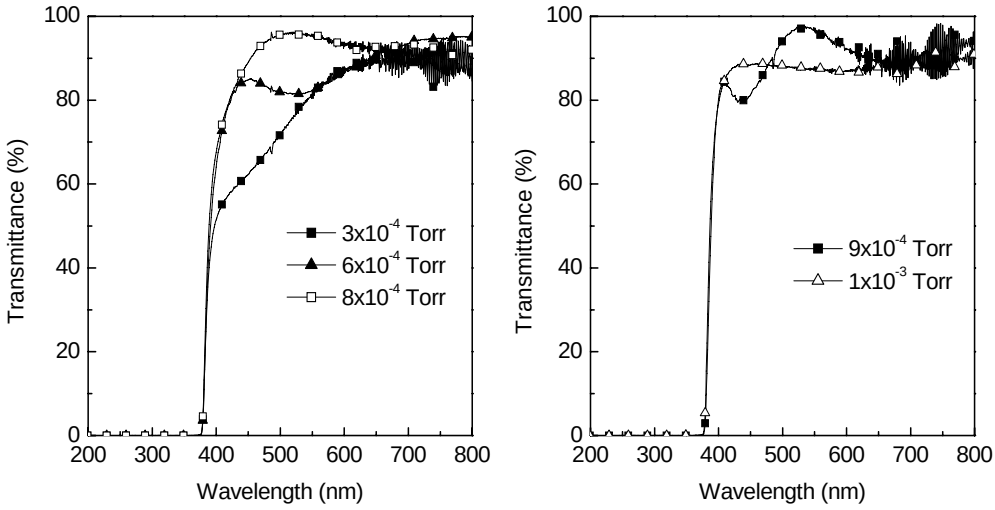

Figure 5.24 Transmittance of ZnO films deposited on polymer substrates.

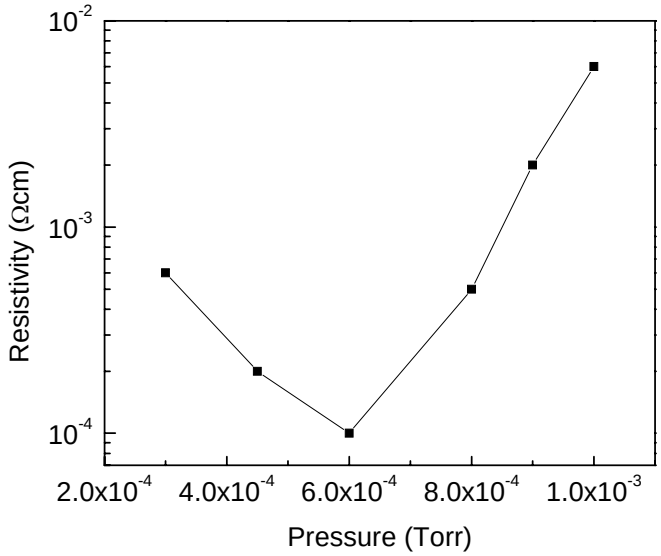

Figure 5.25 Resistivity of ZnO:Al films as a function of oxygen pressure.

5.5 Conclusions

A thorough characterization of ZnO films has been carried out in the following aspects: crystallinity, internal stress, surface morphology, electrical properties, photoluminescence, transmittance, and absorption. The ZnO and ZnO:Al films deposited by the FCVA (under the appropriate growth parameters) have both characteristics of high transmittance and low resistivity, therefore it is suitable for use as transparent conducting oxide. Furthermore, the films that are deposited at moderate substrate temperatures (300°C or above) are of high quality, as evidenced by XRD and optical characterization. In fact, ultraviolet amplified spontaneous emission from zinc oxide ridge waveguides on silicon substrate has been achieved using the ZnO films deposited by the FCVA. [87] In addition to the abovementioned attributes, it is also possible to use our ZnO film as the active channel layer in a transparent thin film transistor.

Chapter 6

Fabrication and Characterization of Transparent ZnO-based Thin Film Transistors

6.1 Device Fabrication

The structure of the TFT under discussion is as follows:

- 2 ITO electrodes grown on glass are used as the drain and source.
- ZnO is the active layer.
- MgO is used as gate insulator layer (also deposited by FCVA).
- Highly conductive ZnO is used as the gate electrode.

Characteristics of Magnesium Oxide as gate insulator

MgO has the following advantages: (1) possesses a wide band gap, (2) is highly ionic, (3) a good insulator, (4) chemically stable. Due to all these suitable properties, it has found itself as protecting layers of dielectric to improve the discharge characteristics and panel's lifetime in an ac-plasma display panel. [88] It has good transparency as well, which makes it a suitable candidate as the gate oxide layer in a transparent thin film transistor. It has a very high resistivity, which is due to the high crystalline quality and less defects in the polycrystalline film. The properties listed make MgO the choice for the insulating layer for the TTFT.

Below is a flow chart diagram that gives a brief overview on the steps involved for growing this top gate transparent thin film transistor.

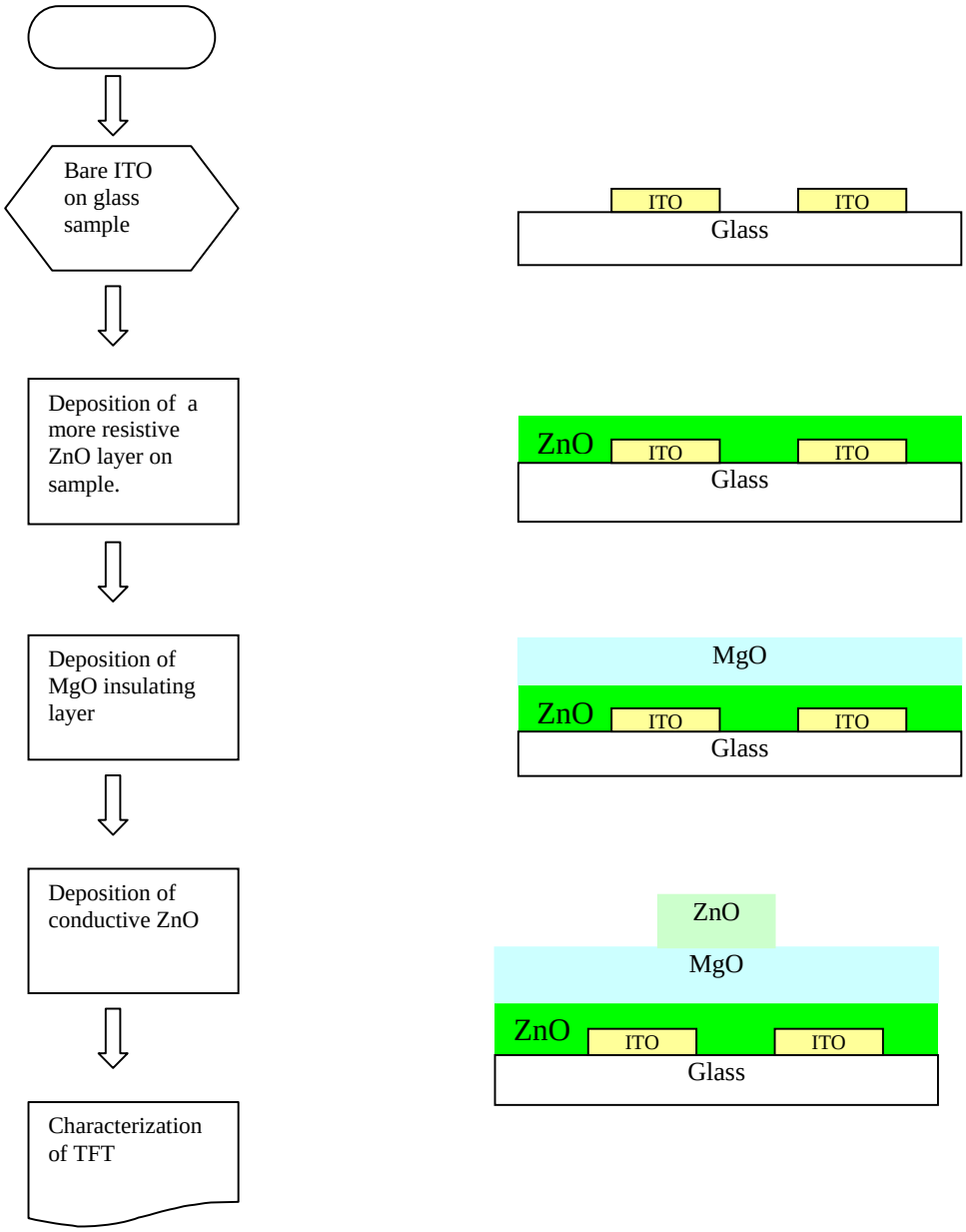

Figure 6.1 Flow Diagram of full fabrication process.

6.2 Electrical Characterization

6.2.1 Characterization of ZnO channel layer

The resistivity of ZnO film deposited on glass substrate without ITO (indium tin oxide) has already been discussed in Section 5.2. However, for the TTFT structure, when ZnO is deposited on top of ITO, the ZnO film in the narrow region of the channel may become more conductive, perhaps due to diffusion of indium into the ZnO layer. As a result of this, we must characterize the resistance through the 2 ITO electrodes, i.e. the resistance between source and drain.

From the knowledge that current will flow through the least resistive and shortest path, and that glass is an insulating material, a safe assumption can be made that the resistance is the area of concern as shown in Figure 6.2.

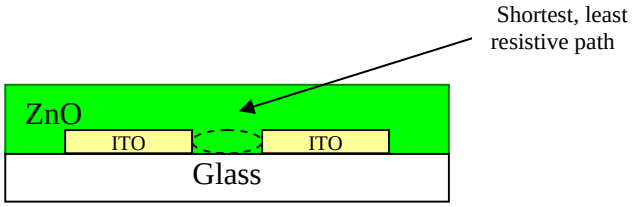

Figure 6.2 Least Resistive Path

The resistance of the active channel layer should preferably be in the MΩ range. It was found that our as-grown films deposited on ITO-coated glass yielded a low source-to-drain resistance. This would lead to device failure as that would mean the transistor will always be in the “on” state. That is, there will be electrical conduction between source

and drain even when no gate voltage is applied. To increase the resistance between source and drain, the following measures were taken: 1) introduce more oxygen into the chamber during deposition; 2) anneal the sample. Both measures work through reducing the amount of interstitial zinc, and hence the carrier concentration. Annealing at 300°C was performed on the films at various durations, and the results are reflected in table 6.1.

Table 6.1: Effect of annealing on source-to-drain resistance

Annealing time (min)	Resistance of channel (Source-Drain) (MΩ)
0	0.8
10	0.816
20	0.96
40	2.23
60	14.9
120	24.8

Furthermore, it was found that after depositing the MgO gate oxide layer, the properties of the ZnO layer changed again. The solution to this problem is same as above, that is, to perform annealing. Subsequently, all TTFT structures were annealed at 300°C for 120 min.

6.2.2 Characterization of complete TFT

Using the Semiconductor Parameter Analyzer HP6102 Precision, three probes were connected to the sample.

1st probe ——————————— input variable of V_{gate} (-5 to 40 V)

2nd probe ——————————— constant V_{drain} (10V)

3rd probe ——————————— common ground V_{source}

However, the gate leakage current was not monitored when the I_{ds} measurement was performed.

The graph of the drain current was plotted against the gate voltage as shown in Figure 6.3.

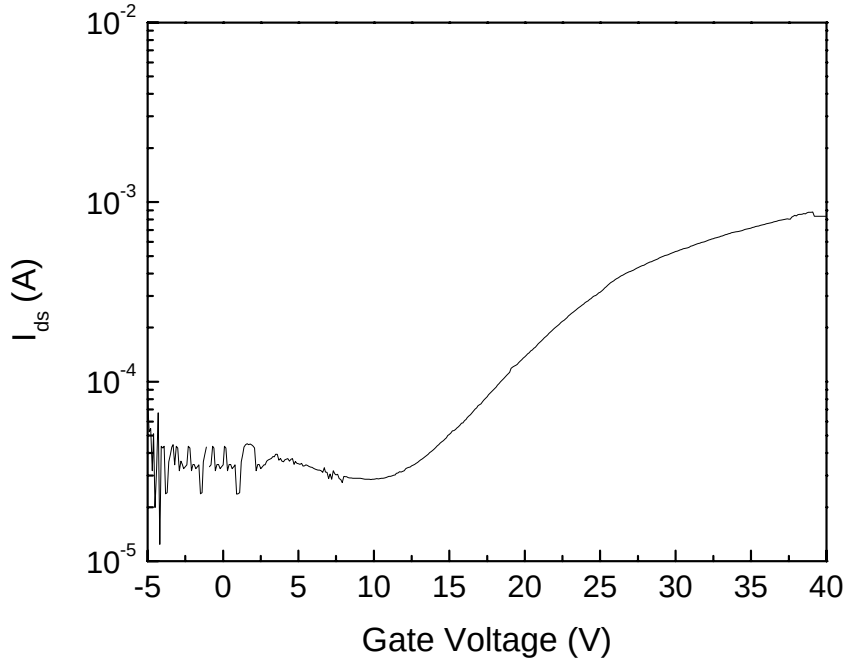

Figure 6.3 Transfer characteristics of the TTFT for V_{ds} =10V.

Leakage current 31.8μA

V_{th} 11.3 V

I_{on}/I_{off} 28.1

A field effect mobility (μ_{FE}) of about 0.005 $cm^2V^{-1}s^{-1}$ was obtained using the following equation:

$$\sqrt{I_D} = (V_G - V_{th})\sqrt{C_0 . \mu_{FE} . W / 2L} \qquad (13)$$

where I_D = saturation current

V_G = Gate voltage

V_{th} = threshold voltage

C_o = Capacitance of gate insulator = 9.7

W = Width of channel = 3621 µm

L = Length of channel = 577 µm

6.3 Optical Characterization

From figures 6.4 and 6.5, it can be seen that our TTFTs are highly transparent, hence fulfilling one of the major requirements of TTFTs.

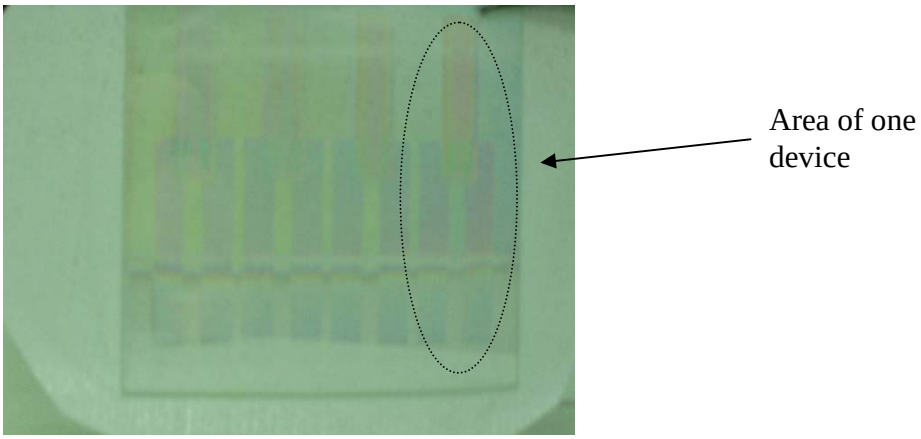

Figure 6.4 Physical appearance of ZnO-based TTFT.

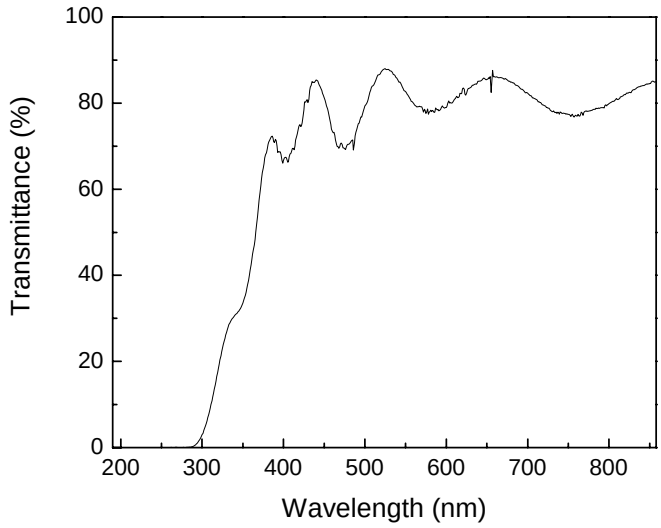

Figure 6.5 Optical transmittance for TTFT structure (including substrate).

6.4 Conclusions

The transparency requirement of a transparent thin film transistor has been satisfied, as the transmittance of our TTFT is 80%. The TTFT fabricated is a low performance one for the following reasons: (1) the I_{on}/I_{off} ratio of 28 is too low, a more reasonable figure would be 10^5; (2) the leakage current at 31.8μA is too large. One possible reason is the diffusion of MgO into the ZnO or vice versa. As this is the first time cathodic arc deposition of any variation has been used to fabricate a thin film transistor, much more research needs to be done to fine tune the system. Further research needs to be done to find the optimal growth conditions for fabricating a TTFT using the FCVA.

Chapter 7

Conclusions and Recommendations for Future Work

7.1 Conclusions

The goal of this thesis has been to provide an investigation into the feasibility of growing high quality ZnO films by the FCVA technique. Furthermore, the application of ZnO films in the areas of transparent conducting oxide (TCO), and transparent thin film transistors (TFT) were studied.

To this end, several characterization techniques were employed to investigate the properties of the films. The conclusions to be drawn from these characterization procedures are summarized as follows:

- The quality of the films was verified by the XRD results, which showed the films were preferentially oriented in the (002) direction (as has been reported by many authors using other deposition methods), and had good crystalline quality (as indicated by a strong peak).
- The micrograph obtained from SEM confirms that the films have columnar structure, and there was no void in the films.

- The film's internal stress was studied. It was found to vary with the deposition parameters: (1) the oxygen pressure, (2) substrate bias voltage, and (3) substrate temperature. Hence, it is possible to obtain low-stress films through optimizing the growth parameters, which is of great significance to the applications on polymer substrates (e.g. electronic device on plastic).
- Highly transparent and conductive ZnO:Al films were obtained with resistivity as low as 8×10^{-4} Ωcm, and the transmittance was close to 90% in the visible spectrum. This verifies the possibility of using our films as transparent conducting oxide.
- Optical characterization indicated the optical band gap of the films could be adjusted, both with and without doping. The shift in band gap was attributed to the Burstein-Moss shift.
- The films' reflection of infrared radiation was found to be enhanced by doping with aluminum. This has potential application as electrochromic coating on architectural glazing and heat mirror, etc.

A preliminary study was performed on the fabrication of a ZnO-based transparent thin film transistor. Although the performance of the device (with an I_{on}/I_{off} ratio of 28) was less than desirable, it paved the way for future work as it did show transfer characteristic of transistor, i.e. there is a threshold voltage that causes an increase in the drain current. This demonstrated the feasibility of fabricating a ZnO-based thin film transistor by the FCVA technique.

7.2 Recommendations for Future Work

Further work may be done on the growth of ZnO thin films on polymer substrates to investigate the effect of stress from bending of the substrates. For example, if ZnO were used as a conductor, the electrical conductivity of the film may be monitored as the polymer is bent, to evaluate how much stress the film can sustain before degradation in conductivity becomes significant, such that the electrode fails.

For the fabrication of ZnO-based thin film transistors, it may be necessary to explore other materials as the gate insulator layer, as there seems to be diffusion from MgO to ZnO (another possibility is that the optimal growth condition for MgO needs to be found). This is believed to be the main cause behind the low performance of the TFT, with high leakage current and a low I_{on}/I_{off} ratio. Although thermal annealing improved the situation, it does not completely solve the problem. Furthermore, annealing contradicts our higher objective of growing the films on polymer to create electronics on plastics. It is desirable to optimize the system such that the fabrication of TFT be performed without annealing, hence allowing the use of polymer substrates.

Another area of interest would be the growth of p-type ZnO, paving the way for a ZnO laser diode. Investigation of the lasing effect in ZnO fabricated by the FCVA technique is already in progress by the colleagues of the author, although the author is not directly involved. And results in this area suggests a promising future in the ZnO films prepared

by the FCVA, as attested by the published work (on lasing effect) of this research group.[89, 90]

Furthermore, it is necessary to study the optical band gap engineering of ZnO, i.e. the modification of band gap through doping. This is so as most laser diodes use a quantum well structure to confine the optical energy in the active layer where stimulated emission takes place. For this purpose, besides doping ZnO with Al, future work should be done on doping with Mg and other materials for optical band gap engineering.

Author's Publications

1 H. W. Lee, S. P. Lau, Y. G. Wang, B. K. Tay, and H. H. Hng, "*Internal stress and surface morphology of zinc oxide thin films deposited by filtered cathodic vacuum arc technique*", Thin Solid Films, vol. 458, 15 (2004).

2 H. W. Lee, S. P. Lau, Y. G. Wang, K. Y. Tse, H. H. Hng, and B. K. Tay, "*Structural, electrical and optical properties of Al-doped ZnO thin films prepared by filtered cathodic vacuum arc technique*", Journal of Crystal Growth. (in press)

3 H. W. Lee, Y. G. Wang, S. P. Lau, and B. K. Tay, "*Low temperature deposition of Zinc Oxide films*", Materials Research Society Symposium Proceedings vol. 763, B5.16 (2003).

4 S. F. Yu, Clement Yuen, S. P. Lau, Y. G. Wang, H. W. Lee, and B. K. Tay, "*Ultraviolet amplified spontaneous emission from zinc oxide ridge waveguides on silicon substrate*", Applied Physics Letters, vol. 83, 4288 (2003).

5 Y. G. Wang, S. P. Lau, H. W. Lee, S. F. Yu, B. K. Tay, X. H. Zhang, K. Y. Tse, and H. H. Hng, "*Comprehensive study of ZnO films prepared by filtered cathodic vacuum arc at room temperature*", Journal of Applied Physics, vol. 94, 1597 (2003).

6 Y. G. Wang, S. P. Lau, H. W. Lee, S. F. Yu, B. K. Tay, X. H. Zhang, and H. H. Hng, "*Photoluminescence study of ZnO films prepared by thermal*

oxidation of Zn metallic films in air", Journal of Applied Physics, vol. 94, 354 (2003).

7 S. F. Yu, Clement Yuen, S. P. Lau, and H. W. Lee, "*Zinc oxide thin-film random lasers on silicon substrate*", Applied Physics Letters, vol. 84, 3244 (2004).

8 Y. G. Wang, S. P. Lau, X. H. Zhang, H. W. Lee, H. H. Hng, and B. K. Tay, "*Observations of nitrogen-related photoluminescence bands from nitrogen-doped ZnO films*", Journal of Crystal Growth, vol. 252, 265 (2003).

9 Y.G. Wang, S.P. Lau, X.H. Zhang, H.W. Lee, S.F. Yu, and B.K. Tay and H.H. Hng, "*Evolution of visible luminescence in ZnO by oxidation of zinc films*", Chem. Phys. Lett. **375** (2003) 113.

10 Y.G. Wang, S.P. Lau, X.H. Zhang, H.W. Lee, S.F. Yu, B.K. Tay, and H.H. Hng, "*Enhancement of near-band-edge photoluminescence from ZnO films by face-to-face annealing*", J. Crystal Growth **259** (2003) 335.

Bibliography

[1] C. S. Chen, C. T. Kuo, T. B. Wu, and I. N. Lin, "*Microstructures and Electrical Properties of V_2O_5-based Multicomponent ZnO Varistors Prepared by Microwave Sintering Process*", Jpn. J. Appl. Phys. 1 **36**, 1169 (1997).

[2] W. C. Shin and M. S. Wu, "*Growth of ZnO films on GaAs substrates with a SiO_2 buffer layer by RF planar magnetron sputtering for surface acoustic wave applications*", J. Cryst. Growth **137**, 319 (1994).

[3] K. L. Chopra, S. Major, and D. K. Pandya, "*Transparent conductors—A status review*", Thin Solid Films **102**, 1 (1983).

[4] Y. K. Park, J. I. Han, M. G. Kwak, H. Yang, S. H. Ju, and W. S. Cho, "*Time-resolved spectroscopic study of energy transfer in ZnO:$EuCl_3$ phosphors*", J. Lumin. **78**, 87 (1998).

[5] N. J. Dayan, S. R. Sainkar, R. N. Karekar, and R. C. Aiyer, "*Formulation and characterization of ZnO:Sb thick-film gas sensors*", Thin Solid Films **325**, 254 (1998).

[6] R. F. Service, "*Materials Science: Will UV Lasers Beat the Blues?*", Science **276**, 895 (1997).

[7] Z. K. Tang, G. K. L. Wong, P. Yu, M. Kawasaki, A. Ohtomo, H. Koinuma, and Y. Segawa, "*Room-temperature ultraviolet laser emission from self-assembled ZnO microcrystallite thin films*", Appl. Phys. Lett. **72**, 3270 (1998).

[8] K. K. Kim, J. H. Song, H. J. Jung, W. K. Choi, S. J. Park, J. H. Song, and J. Y. Lee, "*Photoluminescence and heteroepitaxy of ZnO on sapphire substrate (0001) grown by rf magnetron sputtering*", J. Vac. Sci. Technol. A **18**, 2864 (2000).

[9] D. M. Bagnall, Y. F. Chen, Z. Zhu, T. Yao, M. Y. Shen, and T. Goto, "*High temperature excitonic stimulated emission from ZnO epitaxial layers*", Appl. Phys. Lett. **73**, 1038 (1998).

[10] F. Siah, Z. Yang, Z. K. Tang, G. K. L. Wong, M. Kawasaki, A. Ohtomo, H. Koinuma, and Y. Segawa, "*In-plane anisotropic strain of ZnO closely packed microcrystallites grown on tilted (0001) sapphire*", J. Appl. Phys. **88**, 2480 (2000).

[11] K. Haga, F. Katahira, and H. Watanabe, "*Preparation of ZnO films by atmospheric pressure chemical-vapor deposition using zinc acetylacetonate and ozone*", Thin Solid Films **343**, 145 (1999).

[12] A. Hachigo, H. Nakahata, K. Higaki, S. Fujii, and S. Shikata, "*Heteroepitaxial growth of ZnO films on diamond (111) plane by magnetron sputtering*", Appl. Phys. Lett. **65**, 2556 (1994).

[13] M. Hiramatsu, K. Imaeda, N. Horio, and M. Nawata, "*Transparent conducting ZnO thin films prepared by XeCl excimer laser ablation*", J. Vac. Sci. Technol. A **16**, 669 (1998).

[14] K. Badeker, Ann. Phys. (Leipzig), **22**, 749 (1907).

[15] R. L. Hoffman, Thesis: "*Development, Fabrication, and Characterization of Transparent Electronic Devices*", Oregon State University, pp. 3 (2003).

[16] H. Kawazoe, M. Yasukawa, H. Hyodo, M. Kurita, H. Yanagi, and H. Hosono, "*P-type electrical conduction in transparent thin films of $CuAlO_2$*", Nature, **389**, 939 (1997).

[17] H. Morko, G. B. Gao, M. E. Lin, B. Sverdlov, and M. Burns, "*Large-band-gap SiC, III-V nitride, and II-VI ZnSe-based semiconductor device technologies*", J. Appl. Phys. **76**, 1363 (1994).

[18] H. Yanagi, T. Hase, S. Ibuki, K. Ueda, and H. Hosono, "*Bipolarity in electrical conduction of transparent oxide semiconductor $CuInO_2$ with delafossite structure*", Appl. Phys. Lett. **78**, 1583 (2001).

[19] K. H. Kim, K. C. Park, and D. Y. Ma, "*Structural, electrical and optical properties of aluminum doped zinc oxide films prepared by radio frequency magnetron sputtering*", J. Appl. Phys. **81**, 7764 (1997).

[20] P. F. Carcia, R. S. McLean, M. H. Reilly, and Z. G. Li, "*Low-stress indium–tin–oxide thin films rf magnetron sputtered on polyester substrates*", Appl. Phys. Lett. **81**, 1800 (2002).

[21] X. T. Hao, J. Ma, D. H. Zhang, Y. G. Yang, H. L. Ma, C. F. Cheng and X. D. Liu, "*Comparison of the properties for ZnO:Al films deposited on polyimide and glass substrates*", Materials Science and Engineering B **90**, 50 (2002).

[22] M. Hiramatsu, K. Imaeda, N. Horio, and M. Nawata, "*Transparent conducting ZnO thin films prepared by XeCl excimer laser ablation*", J. Vac. Sci. Technol. A **16**, 669 (1998).

[23] H. Kim, J. S. Horwitz, S. B. Qadri, and D. B. Chrisey, "*Epitaxial growth of Al-doped ZnO thin films grown by pulsed laser deposition*", Thin Solid Films **420**, 107 (2002).

[24] C. R. Kagan, and P. Andry, "*Thin Film Transistors*", Marcel Dekker, Inc., pp. 139 (2003).

[25] F. Garnier, G. Horowitz, X. Z. Peng, and D. Fichou, "*An all-organic "soft" thin film transistor with very high carrier mobility*", Adv. Mater. **2**, 592 (1990).

[26] H. Klauk, M. Halik, U. Zschieschang, G. Schmid, W. Radlik, and W. Weber, "*High-mobility polymer gate dielectric pentacene thin film transistors*", J. Appl. Phys., **92**, 5259 (2002).

[27] M. W. J. Prins, K. Grosse-Holz, G. Miller, J. F. M. Cillessen, J. B. Giesbers, R. P. Weening, and R. M. Wolf, "*A ferroelectric transparent thin-film transistor*", Appl. Phys. Lett., **68**, 3650 (1996).

[28] K. Grosse-Holz, J. F. M. Cillessen, M. W. J. Prins, P. W. M. Blom, R. M. Wolf, L. F. Feiner, and R. Waser, "*Semiconductive behaviour of Sb doped SnO_2 thin films*", Mat. Res. Soc. Symp. Proc., **401**, 67 (1996).

[29] R. L. Hoffman, B. J. Norris, and J. F. Wager, "*ZnO-based transparent thin-film transistors*", Appl. Phys. Lett. **82**, 733 (2003).

[30] S. Masuda, K. Kitamura, Y. Okumura, and S. Miyatake, "*Transparent thin film transistors using ZnO as an active channel layer and their electrical properties*", J. Appl. Phys., **93**, 1624 (2003).

[31] K. Nomura, H. Ohta, K. Ueda, T. Kamiya, M. Hirano, H. Hosono, "*Thin-Film Transistor Fabricated in Single-Crystalline Transparent Oxide Semiconductor*", Science, **300**, 1269 (2003).

[32] A. Anders, "*Energetic deposition using filtered cathodic arc plasmas*", Vacuum **67**, 673 (2002).

[33] B. Juttner, V. F. Puchkarev, E. Hantzsche, I. Beilis, "*Handbook of vacuum arc science and technology*", Park Ridge, NJ: Noyes, pp. 73 (1995).

[34] A. Anders, B. Yotsombat, R. Binder, "*Correlation between cathode properties, burning voltage, and plasma parameters of vacuum arcs*", J. Appl. Phys. **89**, 7764 (2001).

[35] G. F. You, Thesis: "*Modeling and Characterization of Double Bend Filtered Cathodic Vacuum Arc System*", Nanyang Technological University, pp. 1 (2001).

[36] I. G. Brown, "*Cathodic arc deposition of films*", Annu. Rev. Mater. Sci. **28**, 243 (1998).

[37] II Aksenov, S. I. Vakula, V. G. Padalka, "*High-efficiency source of pure carbon plasma*", Sov. Phys. Tech. Phys. **25**, 1164 (1980).

[38] II Aksenov, V. A. Belous, V. G. Padalka, V. M. Khoroshikh, "*Transport of plasma streams in a curvilinear plasma-optics system*", Sov. J. Plasma Phys. **4**, 425 (1978).

[39] II Aksenov, A. N. Belokhvostnikov, V. G. Padalka, N. S. Repalov, V. M. Khoroshikh, "*Plasma flux motion in a toroidal plasma guide*", Plasma Phys. Control. Fusion **28**, 761 (1986).

[40] S. Anders, A. Anders, and I. G. Brown, "*Focused injection of vacuum arc plasmas into curved magnetic filters*", J. Appl. Phys. **75**, 4895 (1994).

[41] A. Anders, S. Anders, and I. G. Brown, "*Effect of duct bias on transport of vacuum arc plasmas through curved magnetic filters*", J. Appl. Phys. **75**, 4900 (1994).

[42] A. Anders, S. Anders, and I. G. Brown, "*Transport of vacuum arc plasmas through magnetic macroparticle filters*", Plasma Sources Sci. Technol. **4**, 1 (1995).

[43] S. Anders, A. Anders, M. R. Dickinson, R. A. MacGill, I. G. Brown, "*S-Shaped Magnetic Macroparticle Filter for Cathodic Arc Deposition*", IEEE Trans. Plasma Sci. **25**, 670 (1997).

[44] L. Jr. Spitzer, "*Physics of Fully Ionized Gases*", New York: Wiley-Interscience, pp. 3-9 (1965).

[45] F. F. Chen, "*Introduction to Plasma Physics*", New York: Plenum, pp. 23-26 (1974).

[46] C. S. Bhatia, S. Anders, K. Bobb, R. Hsiao, D. B. Bogy, and I. G. Brown, "*Ultra-thin overcoats for the head/disk interface tribology*", J. Tribol. **120**, 795 (1998).

[47] S. Anders, I. G. Brown, C. S. Bhatia, and D. B. Bogy, "*Cathodic Arc Deposited Diamond-like Carbon Films for Hard-Disk Tribology Applications*", Data Storage, pp. 31 (1997).

[48] T. Schulke, A. Anders, P. Siemroth, "*Macroparticle filtering of high-current vacuum arc plasmas*", IEEE Trans. Plasma Sci. **25**, 660 (1997).

[49] A. I. Ryabchikov, I. B. Stepanov, "*Investigations of forming metal-plasma flows filtered from microparticle fraction in vacuum arc evaporators*", Rev. Sci. Instrum. **69**, 810 (1998).

[50] A. I. Ryabchikov, I. B. Stepanov, S. V. Dektjarev, O. V. Sergeev, "*Vacuum arc ion and plasma source Raduga 5 for materials treatment*", Rev. Sci. Instrum. **69**, 893 (1998).

[51] S. Anders, A. Anders, M. Rubin, Z. Wang, S. Raoux, F. Kong, and I. G. Brown, "*Formation of metal oxides by cathodic arc deposition*", Surface Coatings Technol. **76-77**, 167 (1995).

[52] B. L. Gabriel, "*SEM: A User's Manual for Materials Science*", American Society for Metals (1985).

[53] K. D. Mielenz, "*Optical Radiation Measurements, Vol. 3, Measurement of Photoluminescence*", Academic Press, Inc. (Harcourt Brace Jovanovich, Publishers) (1982).

[54] X. Jiang, C. L. Jia, and B. Szyszka, "*Manufacture of specific structure of aluminum-doped zinc oxide films by patterning the substrate surface*", Appl. Phys. Lett. **80**, 3090 (2002).

[55] M. Chen, Z. L. Pei, X. Wang, C. Sun and L. S. Wen, "*Structural, electrical, and optical properties of transparent conductive oxide ZnO:Al films prepared by dc magnetron reactive sputtering*", J. Vac. Sci. Technol. A **19**, 963 (2001).

[56] T. A. Polley and W. B. Carter, "*Zone model for zinc oxide deposited by combustion chemical vapor deposition*", Thin Solid Films **384**, 177 (2001).

[57] J. A. Thornton, "*The microstructure of sputter-deposited coatings*", J. Vac. Sci. Technol. A **4**, 3059 (1986).

[58] E. Mirica, G. Kowach, and H. Du, "*Modified Structure Zone Model to Describe the Morphological Evolution of ZnO Thin Films Deposited by Reactive Sputtering*", Crystal Growth and Design **4**, 157 (2004).

[59] J. Hinze and K. Ellmer, "*In situ measurement of mechanical stress in polycrystalline zinc-oxide thin films prepared by magnetron sputtering*", J. Appl. Phys. **88**, 2443 (2000).

[60] S. J. Bull, A. M. Jones, and A. R. McCabe, "*Residual stress in ion-assisted coatings*", Surf. Coat. Technol. **54**, 173 (1992).

[61] S. M. Sze, "*Semiconductor Devices Physics and Technology*", Wiley, 538 (2002).

[62] D. W. Hoffman and J. A. Thornton, "*The compressive stress transition in Al, V, Zr, Nb and W metal films sputtered at low working pressures*", Thin Solid Films **45**, 387 (1977).

[63] L. Parfitt, M. Goldiner, J. W. Jones, and G. S. Was, "*Residual stresses in amorphous alumina films synthesized by ion beam assisted deposition*", J. Appl. Phys. **77**, 3029 (1995).

[64] H. Miura and N. Okamoto, "*Crystallization-induced stress in phosphorus-doped amorphous silicon thin films*", J. Appl. Phys. **75**, 4747 (1994).

[65] H. Miura, H. Ohta, and N. Okamoto, "*Crystallization-induced stress in silicon thin films*", Appl. Phys. Lett. **60**, 2746 (1992).

[66] C. A. Davis, "*A simple model for the formation of compressive stress in thin films by ion bombardment*", Thin Solid Films **226**, 30 (1993).

[67] H. Windischmann, "*An intrinsic stress scaling law for polycrystalline thin films prepared by ion beam sputtering*", J. Appl. Phys. **62**, 1800 (1987).

[68] H. Windischmann, "*Intrinsic stress in sputter-deposited thin films*", Crit. Rev. Solid State Mater. Sci. **17**, 547 (1992).

[69] D. C. Look, "*Recent advances in ZnO materials and devices*", Mater. Sci. Eng., B **80**, 383 (2001).

[70] F. A. Kroger, "*The Chemistry of Imperfect Crystals*", North-Holland, Amsterdam (1974).

[71] D. C. Look, J. W. Hemsky, and J. R. Sizelove, "*Residual Native Shallow Donor in ZnO*", Phys. Rev. Lett. **82**, 2552 (1999).

[72] F. D. Auret, S. A. Goodman, M. J. Legodi, and W. E. Meyer, "*Electrical characterization of vapor-phase-grown single-crystal ZnO*", Appl. Phys. Lett. **80**, 1340 (2002).

[73] S. B. Zhang, S. H. Wei, and A. Zunger, "*Intrinsic n-type versus p-type doping asymmetry and the defect physics of ZnO*", Phys. Rev. B **63**, 075205 (2001).

[74] C. G. Van de Walle, "*Hydrogen as a Cause of Doping in Zinc Oxide*", Phys. Rev. Lett. **85**, 1012 (2000).

[75] D. M. Hoffman, A. Hofstaetter, F. Leiter, H. Zhou, F. Henecher, B. K. Meyer, S. B. Orlinskii, J. Schmidt, and P. G. Baranov, "*Hydrogen: A Relevant Shallow Donor in Zinc Oxide*", Phys. Review Lett. **88**, 045504 (2002).

[76] S. F. Cox *et al.*, "*Experimental Confirmation of the Predicted Shallow Donor Hydrogen State in Zinc Oxide*", Phys. Rev. Lett. **86**, 2601 (2001).

[77] C. Kittle, "*Introduction to Solid State Physics*", Wiley, New York (1986).

[78] Z. L. Pei, C. Sun, M. H. Tan, J. Q. Xiao, D. H. Guan, R. F. Huang, and L. S. Wen, "*Optical and electrical properties of direct-current magnetron sputtered ZnO:Al films*" J. Appl. Phys. **90**, 3432 (2001).

[79] Y. Igasaki and H. Saito, "*Substrate temperature dependence of electrical properties of ZnO:Al epitaxial films on sapphire (1$\bar{2}$10)*", J. Appl. Phys. **69**, 2190 (1991).

[80] Z. C. Zin, I. Hamberg, and C. G. Granqvist, "*Optical properties of sputter-deposited ZnO:Al thin films*", J. Appl. Phys. **64**, 5117 (1988).

[81] T. Minami, H. Nanto, and S. Takata, "*Optical Properties of Aluminum Doped Zinc Oxide Thin Films Prepared by RF Magnetron Sputtering*", Jpn. J. Appl. Phys. **24**, L605 (1985).

[82] E. Burstein, "*Anomalous Optical Absorption Limit in InSb*", Phys. Rev. **93**, 632 (1954).

[83] X. L. Wu, G. G. Siu, C. L. Fu, and H. C. Ong, "*Photoluminescence and cathodoluminescence studies of stoichiometric and oxygen-deficient ZnO films*", Appl. Phys. Lett. **78**, 2285 (2001).

[84] K. Vanheusden, W. L. Warren, C. H. Seager, D. R. Tallant, J. A. Voigt, and B. E. Gnade, "*Mechanisms behind green photoluminescence in ZnO phosphor powders*", J. Appl. Phys. **79**, 7983 (1996).

[85] Z. L. Pei, C. Sun, M. H. Tan, J. Q. Xiao, D. H. Guan, R. F. Huang, and L. S. Wen, "*Optical and electrical properties of direct-current magnetron sputtered ZnO:Al films*", J. Appl. Phys. **90**, 3432 (2001).

[86] G. Frank, E. Kauer, and H. Kostlin, "*Transparent heat-reflecting coatings based on highly doped semiconductors*", Thin Solid Films **77**, 107 (1981).

[87] S. F. Yu, Clement Yuen, S. P. Lau, Y. G. Wang, H. W. Lee, and B. K. Tay, "*Ultraviolet amplified spontaneous emission from zinc oxide ridge waveguides on silicon substrate*", Appl. Phys. Lett. **83**, 4288 (2003).

[88] T. W. Kim, and Y. S. You, "*Microstructural and electrical properties of MgO thin films grown on p-InP (100) substrates at low temperature*", Appl. Surface Sci. **180**, 162 (2001).

[89] S. F. Yu, Clement Yuen, S. P. Lau, W. I. Park, and Gyu-Chul Yi, "*Random laser action in ZnO nanorod arrays embedded in ZnO epilayers*", Appl. Phys. Lett. **84**, 3241 (2004).

[90] S. F. Yu, Clement Yuen, S. P. Lau, and H. W. Lee, "*Zinc oxide thin-film random lasers on silicon substrate*", Appl. Phys. Lett. **84**, 3244 (2004).